Diploma Thesis

Optimizing Liquid Analysis with QCL-based Multi-Pathlength Mid-IR Spectroscopy

Carried out for the purpose of obtaining the degree of Master of Science
Submitted at TU Wien, Faculty of Technical Chemistry
by

Lisa Riedlsperger

Mat. Nr.: 11827185

under the supervision of

Univ. Prof. Dr. Bernhard Lendl
Dr. Alicja Dabrowska

Institute of Chemical Technologies and Analytics

Vienna, 16 September 2024

Statutory Declaration

I hereby declare that I have completed this diploma thesis independently and that no other aids have been used than those I have cited as sources. Literal and analogous quotations have been marked accordingly.

Vienna, September 2024

Lisa Riedlsperger

Acknowledgement

First of all, I would like to thank Bernhard Lendl for the opportunity to conduct my master's thesis at the CAVS group and for his valuable insights, constructive feedback and strong overall support. I am so very grateful to my supervisor Alicja Dabrowska, not only for her academic support but also for her continuous encouragement.

Furthermore, I would like to acknowledge Agilent Technologies for providing the topic of this work and for their financial backing.

I would also like to express my gratitude to the members of the CAVS group, who have consistently provided motivation and valuable suggestions. I am especially grateful for the support of Leo, Iskander, Felix, and Georg, who kindly offered their assistance with this work. To Adea and Sebi I just want to say thank you for always cheering me up. Without them and the other colleagues from CAVS, in particular Pily, Dani, Lena, Loisi, Shilpa, Verena, Miro, Savda, Ufuk, Yide, Andreas, Alex, Conny, Daniel, Davide, Dominik, Elisabeth, Elizandra, Giovanna, Giulia, Gustavo, Harald, Jesús, Margaux, and Paul the time spent here would just not be the same.

Last but not least I would like to thank my family and friends for their love, encouragement and endless support. A very special thank you goes to Sebastian, who has always been there for me.

Abstract

Mid-infrared spectroscopy with a fixed transmission pathlength represents a well-established methodology for the analysis of solutes in liquids. The choice of the pathlength to be used is governed mainly by the solvent absorption in the spectral region of interest. For achieving highest sensitivity large pathlength are preferred. However, the achievable maximum pathlength is dictated by the solvent absorption. As this background absorption is strongly varying across the spectral range of interest, a compromise needs to be made when choosing the pathlength to be employed that balances the need for high sensitivity with the aim of enabling measurements in a broad spectral range without facing total solvent absorption. The use of highly absorbing matrices, such as water, restricts the optical pathlength to a minimum. This is especially important as water is abundant, non-toxic, environmentally friendly and naturally the most relevant solvent for biological samples. Unfortunately, the measurement of peptides and proteins in aqueous solution is especially challenging as the amide I (1700–1600 cm^{-1}) band, which contains information about the secondary structure of proteins, is overlapping with the bending vibration of water dictating very short pathlength in that range despite the fact that longer pathlengths could be tolerated in spectral region of reduced water absorption.

This study presents the development and validation process of a novel external cavity quantum cascade laser-based multi-pathlength spectroscopic setup equipped with a wedge-shaped transmission flow cell and a pyroelectric array detector for mid-infrard spectroscopy. The main innovation lies in the wedge-shaped transmission cell, which allows for simultaneous measurement of liquids across multiple pathlengths. The measurements, conducted with caffeine in ethanol and aqueous solutions of caffeine and bovine serum albumin, demonstrated the benefit of simultaneous measurement of multiple pathlengths in two ways. Firstly, the effective dynamic range of the setup, which is typically constrained by the pyroelectric detectors' dynamic range, was increased by allowing the data to be selected for each wavenumber with a distinct pathlength. Secondly, it was demonstrated that a higher signal-to-noise ratio could be achieved with the presented setup by averaging the spectra at their optimal pathlengths, in comparison to spectra at constant pathlengths with the same setup. In order to select the optimal pathlength, the pathlength-to-noise ratio (PNR), was introduced. This new metric allows for the inclusion of the influence of the variable pathlength on the detectability of a substance while maintaining low noise levels. The presented proof of concept for this novel setup should serve as a starting point for further refinements of the concept which could lead to improvements when performing mid-IR spectroscopic measurements of liquids and in particular of solutes in aqueous solutions.

Kurzfassung

Die Infrarot-Spektroskopie mit konstanter optischer Weglänge ist eine weit etablierte Methode zur Analyse von gelösten Stoffen in Flüssigkeiten. Die Wahl der zu verwendenden Schichtdicke richtet sich hauptsächlich nach der Absorption des Lösungsmittels im betreffenden Spektralbereich. Um eine hohe Empfindlichkeit zu gewährleisten, wird der Einsatz von großen Schichtdicken bevorzugt. Die maximal einsetzbare Schichtdicke wird jedoch von der Absorption des Lösungsmittels bestimmt. Da diese Hintergrundabsorption über den entsprechenden Spektralbereich stark variieren kann, muss bei der Wahl der Schichtdicke ein Kompromiss zwischen der erforderlichen Empfindlichkeit und dem Ermöglichen von Messungen eines breiten Spektralbereichs, ohne dass es zur vollständigen Absorption durch das Lösungsmittel kommt, gefunden werden. Die Verwendung von stark absorbierenden Lösungsmitteln wie Wasser schränkt die geeignete Schichtdicke auf ein Minimum ein. Da Wasser jedoch das wichtigste Lösungsmittel von biologischen Proben darstellt, ist die Messung von Peptiden und Proteinen oft eine Herausforderung. Die Amid I-Bande (1700–1600 cm^{-1}) von Proteinen, welche Informationen über die Sekundärstruktur von Proteinen enthält, überschneidet sich mit der Biegeschwingung von Wasser. Aus diesem Grund muss die optische Weglänge in diesem Bereich sehr kurz gewählt werden, obwohl in Spektralbereichen mit geringerer Wasserabsorption längere Weglängen toleriert werden könnten.

In dieser Arbeit wird die Entwicklung und Validierung eines auf einem Quantenkaskadenlaser basierenden spektroskopischen Messaufbaus vorgestellt, welcher mit einer keilförmigen Transmissions-Flusszelle und einem pyroelektrischen Array-Detektor ausgestattet ist. Die Hauptinnovation liegt in der keilförmigen Flusszelle, die eine Messung von Flüssigkeiten über mehrere Schichtdicken ermöglicht. Die Messungen wurden von Koffein in Ethanol und wässrigen Lösungen von Koffein und Rinderserumalbumin durchgeführt und zeigten die Vorteile der simultanen Messung mehrerer Schichtdicken in zweierlei Hinsicht. Erstens wurde der effektive dynamische Bereich des Aufbaus, der normalerweise durch den dynamischen Bereich der pyroelektrischen Detektoren bestimmt ist, vergrößert, indem die Daten für jede Wellenzahl mit einer bestimmten Weglänge selektiert werden konnten. Zweitens wurde gezeigt, dass mit dem vorgestellten Aufbau ein höheres Signal-Rausch-Verhältnis erreicht werden kann als im Vergleich zu Spektren bei konstanten Pfadlängen mit demselben Aufbau, indem die Spektren bei ihren optimalen Pfadlängen gemittelt werden. Um die optimale Weglänge auszuwählen, wurde das Weglängen-Rausch-Verhältnis eingeführt, um den Einfluss der variablen Weglänge bei gleichzeitiger Beibehaltung niedriger Rauschwerte zu berücksichtigen. Der vorgestellte Aufbau sollte als Ausgangspunkt für die weitere Verfeinerungen des Konzepts dienen, die zu Verbesserungen von spektroskopischen Messungen im mittleren IR-Bereich von Flüssigkeiten, insbesondere von gelösten Stoffen in wässrigen Lösungen, führen.

Table of Content

1 Introduction

1.1 Aim of Thesis

Mid-infrared (mid-IR) spectroscopy is a widely used technique for analyzing liquid phase systems, however currently used systems with fixed transmission pathlengths face certain challenges with room for improvement. These challenges are especially apparent when working with highly absorbing solvents such as water. Due to the unevenly absorbing nature of such matrices, conventional setups are forced to use very small pathlengths to avoid total absorption in the region of strongest absorption. Therefore, the application is often restricted to highly concentrated solutions. A good example is measuring proteins in aqueous solution a task which is especially challenging as the amide I (1700–1600 cm^{-1}) band, which contains information about the secondary structure of the protein, is overlapping with the bending vibration of water. As a result, this band is often difficult to be measured accurately and hence difficult to interpret.

These limitations are compounded in case the detectors used have a limited dynamic range, which is the case of the array detector used in this work. For non-uniformly absorbing matrices, the detector may not be able to detect the full range of the spectrum, as the high absorbance of the sample in some parts may result in an undetectable light intensity, or saturation of the detector may occur in regions where the transmission is high. For being able to conduct reliable measurements it is therefore important to stay within the dynamic range of the used detector. While mid-IR detectors with a larger dynamic range than the one used in this thesis do exist, the general need to remain within the linear dynamic range of a given detector holds true for all detector types. These factors, the need for achieving a high sensitivity demanding large pathlength, strong solvent background absorption often dictating short pathlengths and the fact of a limited dynamic range of cost-effective mid-IR detectors call for more adaptable and efficient methods that can overcome the limitations of traditional fixed-pathlength transmission spectroscopy, especially for applications involving highly absorbing solvents such as water.

The objective of this thesis is to address these challenges by developing a novel spectroscopic setup based on quantum cascade laser multi-pathlength mid-IR spectroscopy. By employing a wedged-shaped transmission cell, this approach enables the simultaneous measurement of a range of optical pathlengths, thereby facilitating the analysis of a diverse range of concentrations. Moreover, this configuration permits the measurement of low-absorbing regions with a long pathlength, thereby obtaining a high signal-to-noise ratio for these regions while still enabling the measurement of high-absorbing regions with a reduced sensitivity.

The scope for this work is to develop a setup according to the above-described concept with a multi-pathlength wedge-shaped transmission cell. The individual components of the setup are then to be verified and tested. Furthermore, a Python script is to be developed to operate the setup as well as to allow for the subsequent data processing. The setup is subsequently to be tested with different analytes, with a particular focus on conducting measurements with a protein in aqueous solution to confirm that the setup shows the desired performance characteristics.

1.2 Principles of Infrared Spectroscopy

Spectroscopy is the study of the interaction of matter with electromagnetic radiation through measurement of absorption, scattering or emission of light either in transmission or reflection modalities. Depending on the wavelength and therefore the energy of the radiation, different transitions between quantized energy states can be excited in a molecule. Infrared radiation (between 0.8 and 1000 µm), which induces vibrational transitions, is located in the electromagnetic spectrum between visible light and microwave radiation. As shown in Figure 1, infrared radiation can be divided into the near-infrared (NIR), mid-infrared, and far-infrared regions. The unit used commonly in IR spectroscopy is wavenumber $\tilde{\nu}$, which is defined as the number of wavelength per unit distance (cm^{-1}). [1]

$$\tilde{\nu} = \frac{1}{\lambda} = \frac{\nu}{c} \qquad \text{Equation 1}$$

where λ signifies the wavelength (m), ν refers to the frequency (s^{-1}) and c is the speed of light ($m\ s^{-1}$)

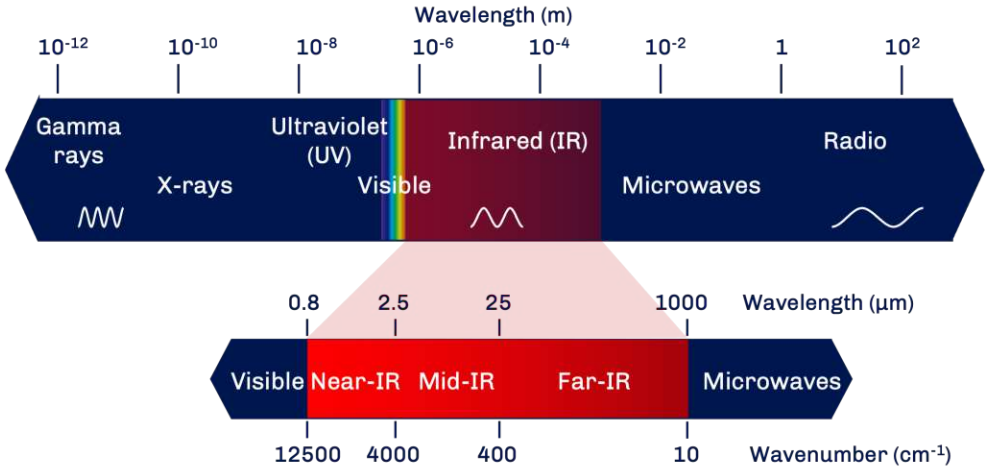

Figure 1: Electromagnetic spectrum with focus on the infrared region.

Measuring substances through IR spectroscopy is principally based on observing the interaction of the molecules to incoming IR radiation by measuring their vibrational response. Each molecule has 3N degrees of freedom in three-dimensional space, where N is the number of atoms. By subtracting the degrees of freedom corresponding to translation in each direction in the coordinate system and rotation about each axis, the number of vibrational modes of a nonlinear molecule (3N – 6) can be determined. Rotation about the molecular axis of a linear molecule does not induce a movement of the atoms, and thus linear molecules have only two degrees of rotational freedom and 3N – 5 vibrational modes. In most cases, not all vibrational modes are discernible in an IR spectrum. This can be attributed to a number of factors, including insufficient absorption, the occurrence of bands absorbing at the same wavelength, or the coalescence of bands with one another. Moreover, for a vibration to be IR-active, meaning to excite a transition in vibrational levels, a change in dipole moment of the whole molecule must occur during the vibration under consideration. [1]

The vibrational modes can be approximated by harmonic displacement from the equilibrium position of the atoms. The harmonic oscillator model offers a straightforward yet effective approximation of the potential energy of a vibrating molecule, in accordance with the Hooke law. The vibrational frequency is thus dependent on both the bond strength and the reduced mass of the two bonded atoms which can be described with Equation 2.

$$\nu = \frac{1}{2\pi}\sqrt{\frac{k}{\mu}} \qquad \text{Equation 2}$$

where k is the effective force constant of the bond, and μ denotes the reduced mass.

Consequently, an increase in bond strength or decrease in reduced mass leads to an increase in frequency. At room temperature, the majority of molecules are in their ground vibrational state ($\nu_i = 0$).[1,2] The energy (ΔE_ν) required for the excitation from the ground state to the first excited state ($\nu_i = 1$) is quantized and corresponds to the energy of the interacting photon. The anharmonic Morse[3] potential offers a superior approximation of the energies of the vibrational modes of a molecule, as it incorporates the influence of bond breaking and repulsion by the positively charged atom nuclei. In contrast to the equidistant energy levels of the harmonic oscillator, the spacing between the energy levels of a Morse potential decreases as the energy approaches the dissociation energy D_e. Under the simple harmonic approximation, changes in ν_i by more than ±1 would not be permitted. However, this restriction does not apply to the anharmonic Morse potential approximation, allowing for the appearance of bands due to non-fundamental vibrations (i.e., overtone and combination vibrations) in the spectrum.

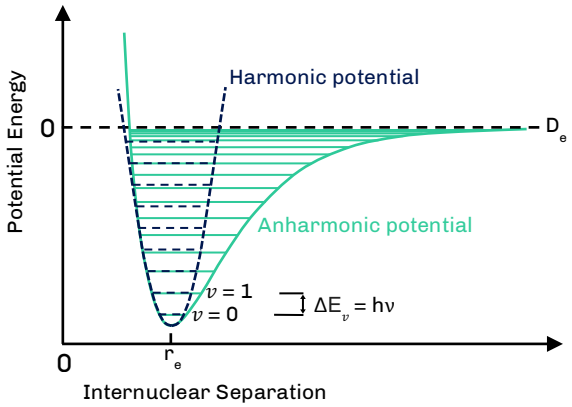

Figure 2: Vibrational energy levels of a harmonic oscillator potential (blue) and a Morse type (anharmonic) oscillator potential (green).

Each normal mode of an oscillating molecule engages a limited number of atoms, resulting in their notable displacement while the remainder of the molecule remains essentially stationary. The fundamental molecular vibrations are of two types: stretching and bending. Stretching vibrations result in an elongation of the bond, whereas bending vibrations (or deformation) entail a change in the bond angle. The fundamental vibrations are illustrated in Figure 2, which demonstrates that stretching can be distinguished into antisymmetric and symmetric stretching. Bending can occur in-plane (i.e., scissoring and rocking) and out-of-plane (i.e., twisting and wagging).[1,4]

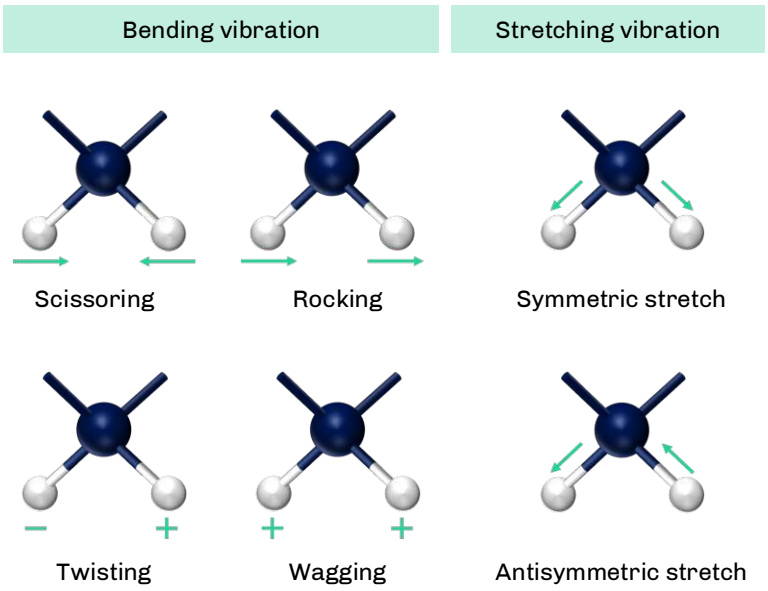

Figure 3: Fundamental vibrational modes: in-plane bending (scissoring and rocking) and out-of-plane bending (twisting and wagging) as well as symmetric and antisymmetric stretching vibrations.

The excitation energy of a vibrational mode depends upon the nature of the bond itself and the surrounding environment. Consequently, each bond will absorb infrared radiation at a wavelength that is characteristic of that particular bond. Fundamental vibrations are primarily observed in the mid-infrared region, where spectral characteristics serve as indicators of specific chemical functional groups present within the molecule. The intensity of a band is determined by the nature of the bond with polar bonds (i.e., C=O, O-H, C-S) exhibiting higher intensity due to the greater dipole change.[2] To excite stretching vibrations typically higher energies are needed than to excite bending vibrations. Consequently, they are observed at higher wavenumbers within the infrared spectrum.[1] Skeletal modes are defined as vibrations that involve the entire molecule and are typically observed in the low wavenumber range of the mid-infrared and far-infrared regions. These vibrations, as well as complex interacting vibrations, produce unique, molecule-specific patterns, making the mid-IR region between 1300 – 400 cm^{-1} known as the "fingerprint" region.[5] The far infrared region, despite the rarity of its application in the field of spectroscopy, can provide valuable insight into the vibrational properties of weak bonds and heavy atoms. In the higher energy NIR region, the primary absorptions are those of overtone and combination vibrations which have significantly smaller absorption coefficients than their fundamental vibrations in the mid-IR range. Although it is typically challenging to assign bands to specific functional groups without extensive chemometric models, NIR spectroscopy is a widely used technique and it is of special relevance in process analytical technology (PAT) applications. Its advantages over mid-infrared include the ability to penetrate through thicker samples without facing total absorption of the incident beam, as well as the availability of more sensitive detectors.[1]

Infrared spectroscopy is a wide field of study and can be applied to the quantitative and qualitative analysis of a variety of samples, including gaseous, liquid, and solid materials. The measurement process is rapid and offers the benefits of being label-free and non-destructive. To date, Fourier-transform infrared (FT-IR) spectrometers are the most commonly used instruments for recording IR spectra (see Section 1.4.1). Infrared spectroscopy employs a multitude of sampling techniques, with the most straightforward being absorption spectroscopy in transmission mode. It is a highly versatile method with a broad range of applications. For example, spectra can be recorded by attenuated total reflection (ATR) by placing the sample on a crystal with a high refractive index (e.g., germanium, diamond, zinc selenide). Another direct sampling technique is dispersion spectroscopy, which entails measuring the phase shift of an electromagnetic wave after it propagates through the sample. In indirect measurements, the IR radiation interacting with the sample is not detected, rather than a change in the medium. Such techniques include photoacoustic and photothermal spectroscopy.

Raman spectroscopy, a method often described as complementary to IR spectroscopy, is based on the principle of inelastic scattering of monochromatic radiation, typically

generated by a laser in the NIR or visible range. It produces a spectrum that is analogous to an infrared absorption spectrum. In contrast to the vibrational transitions observed in infrared spectroscopy, which require a change in the dipole moment, the vibrational bands are only Raman-active if a change in polarizability occurs. To maintain focus on the subject matter within the scope of this work, the discussion will primarily focus on IR spectroscopy of liquid samples in transmission, which will be discussed further in Section 1.3.

1.3 Absorption Spectroscopy in Transmission Mode

Absorption spectroscopy is a technique that can be employed for the analysis of gases, liquids, and solids. In contrast to gas mid-infrared spectroscopy, in which the pathlength can exceed 100 m, liquid spectroscopy is often limited by the absorption of the matrix, with pathlengths typically significantly below 1 mm.[6] In the case of aqueous solutions the maximum pathlength for common spectrometers is as low as 10 µm in order to circumvent total absorption in the region of the water bending vibration ($\tilde{\nu} = 1645\ cm^{-1}$).[7] The construction of flow cells for liquids typically involves the use of two IR-transparent windows (CaF_2, BaF_2, KBr, NaCl) with a PTFE spacer positioned between them and subjected to compression through a metal frame. One window is equipped with two openings, enabling the injection and removal of the liquid. The thickness of the spacer thus defines the pathlength of the cell.

1.3.1 Beer-Lambert Law

The foundation of absorption spectroscopy is the (Bouguer–)Beer–Lambert law (see Equation 3), which describes the exponential intensity decay of monochromatic light passing through a medium. This law relates the attenuation of radiation to the concentration and propagation length within the medium, thereby enabling the determination of analyte concentrations in the sample. Increasing either the concentration or the pathlength will result in higher absorption values and therefore higher absorbance values.

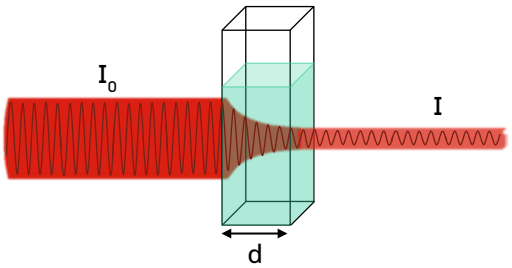

Figure 4: Representation of the decay of intensity (I) of light travelling through a medium with pathlength d.

$$A(\tilde{\nu}) = \log_{10}\frac{I_0}{I} = \varepsilon(\tilde{\nu})\, c\, d \qquad \text{Equation 3}$$

where $A(\tilde{\nu})$ refers to the measured absorbance (AU), I_0 is the initial intensity of the light, I is the intensity after traveling the pathlength d (m), $\varepsilon(\tilde{\nu})$ is the molar (decadic) absorption coefficient ($m^2\ mol^{-1}$), and c denotes the analyte concentration (mol dm^{-3}).

The Beer-Lambert law is an empirical law that does not describe the physical phenomenon of light-matter interaction with absolute precision as it ignores the wave character of electromagnetic radiation. As a result, the interpretation of spectra is often challenging. Accordingly, it is necessary to consider certain limitations when applying the Beer-Lambert law. These limitations arise from chemical interactions, wave optics effects such as interference, and instrumental errors. Firstly, the Beer-Lambert law, which describes a strictly linear dependence of absorbance on concentration, does not accurately represent the reality of high-concentration samples ignoring the fact that the absorbance coefficient is also dependent on the refractive index. Furthermore, also rather than being viewed as separate molecules surrounded by the matrix, electrostatic interactions between the analyte molecules result in a change in the molar absorption coefficient.[8,9] Mayerhöfer and Popp [8] demonstrated that even in the absence of interactions between the molecules, changes in concentration directly impact the dielectric properties and, consequently, the molar absorption coefficient.

The optical conditions also contribute to the formation of the resulting spectrum. In the case of parallel interfaces situated perpendicular to the incident light, a partial reflection of the light will occur that leads to interference effects. In the case of a transmission cell, a minor proportion of the light will be reflected by the second window and subsequently return to the first one, where a further partly reflection will occur. This will result in constructive and destructive interference with the incident beam, depending on the wavelength, pathlength, and refractive index of the sample. The selection of the IR-transparent window material is therefore a crucial decision. Materials like ZnSe or Si will lead to distinct interference patterns and although the interference is not visually discernible with CaF_2 windows, it nevertheless exerts an influence on the recorded spectra.[9-11]

Deviations from the Beer-Lambert law can also be caused by instrumental errors such as instrument misalignment and imperfect optical component, both of which can lead to stray light detection. In addition, real light sources are never strictly monochromatic, causing deviations from the law's assumption of dealing with an even sample absorption within the used spectral resolution, a need which is often summarized by stating that the Beer-Lambert law would require monochromatic radiation. The range in which a linear behavior according to the Beer-Lambert law is observed is highly dependent on the individual components of the setup. The photometric error plays a role at both very high and very low

absorbances. In cases where the absorbance is too high, the detector may not accurately detect the low transmitted energy. Due to the logarithmic relation, small changes in the sample absorbance result in smaller absolute changes in the transmitted beam intensity for large absorbances, so small inaccuracies in the intensity measurement can scale to a relatively large error. Similarly, problems of accurate intensity measurement arise when too high intensities are reaching the detector, and the incident beam intensity is close to the transmitted beam intensity, which is the case of low sample absorbances. To stay within the linear range of the Beer-Lambert law, the sample must often be diluted or concentrated accordingly, or a transmission cell with a more appropriate pathlength must be used.[12]

1.3.2 Qualification and Quantification of IR Measurements

One of the key advantages of mid-infrared spectroscopy is its ability to provide both qualitative and quantitative insights. The band position and form indicate the functional groups present in the sample, while the height and area can be used to determine the concentration of the analyte. While the molar absorption coefficient is tabulated for a multitude of substances in the context of UV-Vis spectroscopy, enabling the direct calculation of concentration via the Beer-Lambert law, this is not the case for mid-infrared spectroscopy. As previously discussed in this chapter, the non-linearity of the Beer-Lambert law, in addition to matrix effects and complex, overlapping absorption bands, makes this approach more challenging.[11] Nevertheless, through the measurement of solutions with a known concentration of the analyte, it is feasible to apply a linear regression. The linear least-square regression is the simplest variant; however, multivariate (or chemometric) methods are becoming increasingly important in this field.

One significant aspect of every spectroscopic measurement is the presence of noise. Noise can be defined as random fluctuations in the baseline of the spectrum. It is not possible to eliminate these unwanted signals entirely, and this represents a limitation of the spectroscopic method in terms of achievable detection limits. The sources of the noise can be, among others, the detector, the radiation source, and the surrounding air or medium. For example, thermal noise originates from the minimal temperature change in the electrical system, while 1/f noise is dependent on the frequency and exhibits a larger magnitude at lower wavenumbers.[13] Bonani and Ghione [14] have shown that the predominant noise effects of a semiconductor detector can be attributed to shot noise, thermal noise, flicker noise, and generation–recombination noise. Consequently, identifying and minimizing the primary source of noise can be challenging.

In the majority of cases, the term noise is defined in terms of the root mean square (RMS) error or standard deviation s_{bl} of the blank measurement.

$$s_{bl} = \sqrt{\frac{\sum(X - x_i)^2}{n}} \qquad \text{Equation 4}$$

where X denotes the mean value of the measured absorbance of the blank measurement, x_i are the individually measured values, and n is the number of data points.

In certain instances, however, the peak-to-peak (p-p) noise is provided, which represents the difference between the highest and lowest peaks across a specific wavenumber region.[15]

In order to evaluate the quality of a system and its measurements, a number of additional parameters have been defined. In addition to determining the concentration of unknown substances, a linear regression can also provide insight into the quality of the system under investigation. The slope m of the regression curve is defined as the sensitivity of the analytical calibration. Consequently, high sensitivity is indicated by a large change in the signal resulting from a minor change in analyte concentration.[16] The calibration curve can be expressed as follows:

$$x = i + mc \qquad \text{Equation 5}$$

where x is the signal or absorbance, i is the intercept and c denotes the concentration.

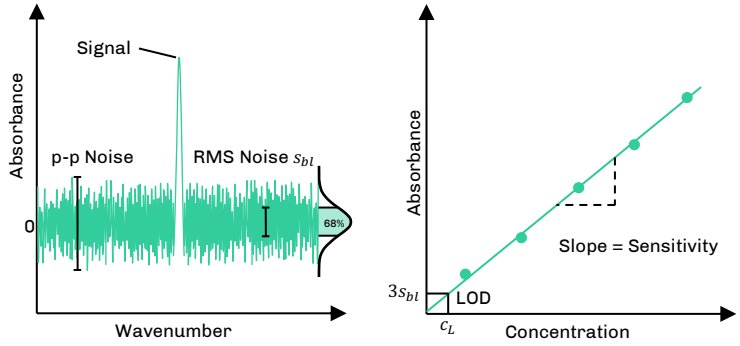

Figure 5: Illustration of signal and noise of a measurement (left), and calibration curve depicting the limit of detection (right).

The limit of detection (LOD) for a given substance (analyte) is determined by the standard deviation of the baseline noise and the slope of a calibration curve constructed for the analyte. The International Union of Pure and Applied Chemistry (IUPAC) defines the LOD as "the smallest measure, x_L, that can be detected with reasonable certainty for a given analytical procedure"[17].

$$x_L = x_{bl} + ks_{bl} \quad \text{Equation 6}$$

where x_{bl} refers to the mean of the blank measurements (AU), k is a numerical factor, and s_{bl} denotes the RMS noise (AU).

The value of k is selected in accordance with the desired confidence level for the detection of the analyte. In the majority of cases, and in compliance with the recommendations set by the IUPAC, the value of k is typically set to 3, which corresponds to a confidence level of 99.86% (one-sided Gaussian).[16-18] Nevertheless, alternative values for k, such as 6, 3.3[19,20] or 2[21], can be found in various sources. The value of LOD in terms of concentration c_L is a function of x_L and can be calculated with the help of the sensitivity.

$$c_L = \frac{x_L - x_{bl}}{m} = \frac{ks_{bl}}{m} \quad \text{Equation 7}$$

Another measure of an instrument's sensitivity is the signal-to-noise ratio. As the name indicates, the signal-to-noise ratio (SNR (-)) is defined as:

$$SNR = \frac{S}{N} \quad \text{Equation 8}$$

where S defines the signal and N is the noise, also given as s_{bl}.

It is essential to provide a detailed method description for acquiring the SNR, as there are various approaches that can be employed. In its most basic form, the signal is defined as the maximum value of the spectral feature, while the noise is represented by the p-p or RMS error of the background, as previously described. A variety of background spectra may be employed to determine the noise at each wavenumber. Noise characteristics of instruments can therefore be given in the time-domain instead of the wavenumber-domain. In the event that this is unavailable, it is recommended that a region in close proximity to the spectral region of the signal be utilized instead.[15] However, the SNR obtained through this method is dependent on the concentration and intrinsic properties of the sample. In order to characterize a spectrometer, a characterization without a sample cell, using 100% transmission as the signal value, is performed. An alternative method for expressing the sensitivity of a spectrometer is to calculate the ratio between the signal power and the noise power. In this context, noise power N' (W) is defined as the noise equivalent power NEP (V W^{-1}), which is the ratio of the root-mean-square noise voltage $V_{s_{bl}}$ (V $Hz^{-1/2}$) to the detector responsivity R_v, per measurement time t (s).

$$NEP = \frac{V_{sbl}}{R_v}$$ Equation 9

$$N' = \frac{NEP}{\sqrt{t}}$$ Equation 10

The responsivity of a detector depends on the type of detector used (i.e., detector material, operation temperature, frequency). The signal power detected for conventional FT-IR spectroscopy using a thermal emitter is proportional to a number of variables, including spectral brightness, throughput, resolution, and efficiency within a specified wavenumber range.

1.3.3 Challenges with Highly Absorbing Solvents

One of the principal factors to be taken into account in mid-IR spectroscopy is the type of solvent employed, as this has a significant impact on the resulting spectra. Solvents typically exhibit absorption bands in the mid-IR region, which can overlap with the bands of the infrared spectra of the analyte. Accordingly, it is preferable to utilize solvents with minimal mid-IR absorption.

However, the selection of a solvent is also constrained by the solubility of the analyte, availability, chemical inertness, and toxicity. For instance, solvents such as carbon tetrachloride, carbon disulfide, and chloroform exhibit minimal absorbance throughout the mid-IR region. Nevertheless, these solvents are known to be toxic and harmful to the environment.

In addition to considerations regarding the properties of the solvents, process efficiency also plays a crucial role. Therefore, it is common practice to measure the sample without sample preparation (e.g. extraction or evaporation) and in-line or on-line of a process. This indicates that, in many cases, there is no viable alternative to the selected solvent for spectroscopy, as modifying it would necessitate considerable additional effort.

The most common solvent - water - is abundant, non-toxic and environmentally friendly and naturally the most relevant solvent for biological samples. However, the major drawback is the broad absorption bands across the IR spectrum. The O-H symmetric and antisymmetric stretching vibrations are partly overlapping and can be found at approximately 3280 cm^{-1} and 3490 cm^{-1} respectively, while the water bending vibration is located near 1645 cm^{-1} (see Figure 6). The libration band correspond to the three hindered rotations (around each axis) restricted by the hydrogen bonding of the water molecules. At approximately 2150 cm^{-1} the relatively weak combination band originates due to anharmonic coupling of the bending vibration with the libration motions.[22]

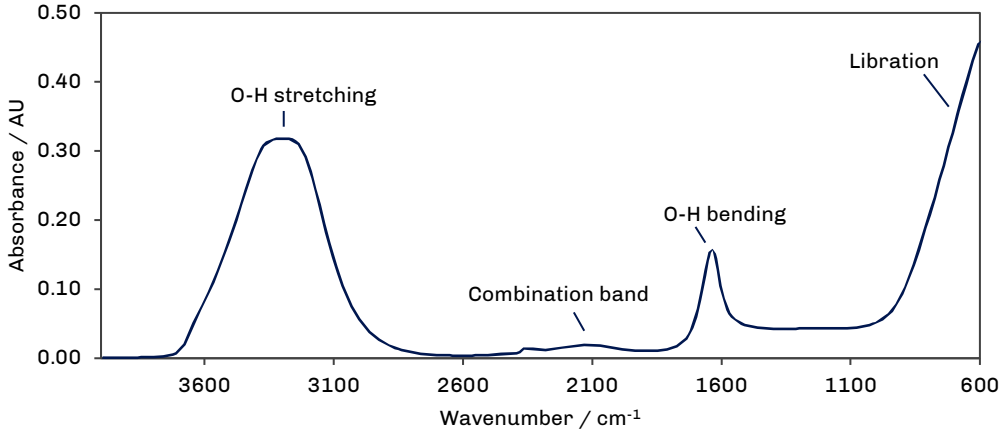

Figure 6: IR spectrum of water with the bands assigned to the respective molecular vibration recorded with an ATR-FT-IR instrument.

To measure aqueous solutions by FT-IR spectroscopy in the region of the water's bending vibration it is necessary to employ very small pathlengths of approximately 10 µm to ensure sufficient throughput. These small pathlengths lead to reduced sensitivity, often making low concentrations undetectable and impose additional physical challenges due to high pressure requirements often leading to leakage in the flow cell.[23]

1.3.4 Implications of Measuring Proteins in Aqueous Solution

The water bending region is of particular significance as a considerable number of important functional groups of organic molecules are absorptive in this region. These include the N-H bending vibration, the alkene C=C vibration, and the C=N vibration of imines.[24] It is also the region of the amide I band (mainly C=O stretching of the amide moiety) of proteins, which are among the most widely studied samples in IR spectroscopy due to high interest in the biomedical field for analyzing the structure and dynamics of proteins.

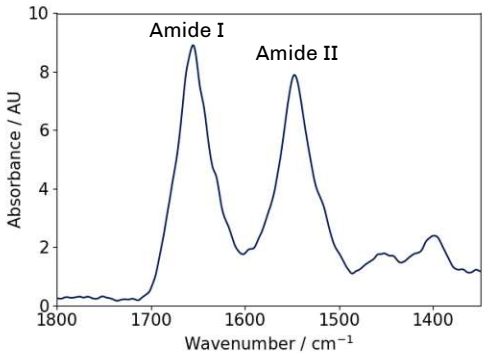

Figure 7: Spectrum of BSA in the amide I and amide II band region, recorded with an FTIR in transmission mode at a pathlength of 7.0 µm.

Proteins display several characteristic bands in the mid-IR region. The peptide backbone of proteins contributes to the majority of absorption with the most prominent bands being the amide I and amide II bands. The amide II band is located between 1600 and 1500 cm^{-1} and originating from the N-H bending and C-N stretching vibration of the peptide bond. Of particular interest is the amide I band, located in the water bending region of 1700–1600 cm^{-1}. The position of the band, which arises from the N-H in-phase bending and C=O stretching vibration, is subject to change due to differing patterns of hydrogen bonding, dipole-dipole interactions, and the geometric orientations of oscillators in a given secondary structure. It is thus possible to distinguish between proteins that are rich in α-helices and those that are rich in β-sheets.[25]

The implications of measuring proteins in aqueous solutions are as follows: The high absorption of water in the region of the amide I band, which provides insights into the secondary structure, results in elevated noise levels at pathlengths appropriate for the amide II bands, which can render the interpretation of the spectra challenging. In contrast, the amide II band, which is frequently employed to determine protein concentration, does not exhibit the same challenges associated with water background absorption. However, it also lacks the capacity to provide information regarding the secondary structure. Moreover, the significant overlap in the amide I region with the bending vibration of water necessitates the use of very small pathlengths in case one aims for high quality spectra in this spectral region. Furthermore, as flow cells with pathlength below 10 µm are difficult to be filled reproducibly, commercial analyzer for protein quantification in milk use pathlengths longer than 25 µm, hence loosing access to the information rich amide I band. [23,26]

1.4 Advancements and Application of Mid-IR Spectroscopy

In the early nineteenth century, the first mid-infrared spectrometer was constructed, marking the beginning of infrared spectroscopy. The subsequent invention of detectors such as the photophone and bolometer in 1881 enabled the first experiments on the composition of the atmosphere. The end of the 19th century marked great advances in the field of IR spectroscopy. The first infrared spectrum was recorded by Abney and Festing, who were able to discern a correlation between the absorbance and the functional groups of a molecule. Although Albert Michelson's and Edward Morley's attempt in 1887[27] to prove the existence of the luminiferous ether was unsuccessful, their invention of the interferometer represented a significant milestone in the history of spectroscopy. Willem H. Julius conducted experiments that led him to the conclusion that the observed absorbance was a consequence of intramolecular motion. William W. Coblentz was able to record the spectra of 120 compounds and concluded that specific bands could be attributed to particular functional groups. His work, although its significance was not immediately recognized, became the standard reference for IR spectra for many years. The possibilities of IR spectroscopy were not recognized until the Second World War, during which IR

spectrometers came to the market. Further improvements, especially in the instrumentation part, followed, but the biggest achievement was the employment of Fourier Transform (FT) infrared spectrometers. The complex calculations, i.e. the Fourier transformation, required to compute spectra from recorded interferograms were only possible to be conducted at reasonable speed after the invention of the computer.[28]

1.4.1 Fourier Transform Infrared Spectroscopy

Prior to the advent of FT-IR spectrometers, dispersive spectrometers were utilized, which employed a monochromator to spatially separate wavelengths of the polychromatic radiation source. In contrast, FT-IR setups utilize an interferometer that generates interference signals by dividing the polychromatic beam and recombining it after the two parts have traveled a different length. While the path length difference is introduced the resulting intensities, which are the result of constructive and destructive interferences of the two beams, are recorded at a detector yielding an interferogram. An FT-IR spectrometer thus enables the simultaneous detection of all wavelengths while the pathlength difference is introduced leading to a high spectral throughput of an average of 50%. Also, the possibility of accepting a circular beam and the absence of narrow slits further increase the throughput in an FT-IR spectrometer compared to a dispersive IR spectrometer. As a consequence FT-IR spectrometer allow to reach high signal-to-noise ratios (SNR) in measurement short time. [1,5]

The majority of FT-IR spectrometers currently available utilize a Globar as the black-body radiation source. A Globar is composed of silicon carbide rods and arches, which are inserted into a circuit. They emit thermal radiation within a range of 4 to 15 µm.[29] The Michelson interferometer is the most commonly utilized configuration and comprises a moving mirror, a fixed mirror, and a beamsplitter. The collimated beam is directed to the beamsplitter, which is a semi-reflective device. Half of the beam is transmitted to the fixed mirror, while the remaining half is reflected towards the moving mirror. The beam components are reflected and subsequently recombined at the beamsplitter. As illustrated in Figure 8, half of the recombined beam will be redirected back to the source, while the other half will proceed to the detector. If the two arms of the interferometer are of equal length, the path difference is zero, and the radiation is in-phase, therefore constructive interference will occur. The mirror will undergo continuous movement, resulting in the occurrence of constructive or destructive interference, dependent on the wavelength and the path difference. If the path difference is an integer multiple of the wavelength, the radiation will be in phase and will interfere constructively. Conversely, the interference minimum will be observed at path differences being multiples of half the wavelength. The use of a broadband radiation source will result in the superimposition of the interference patterns as a function of the retardation. When the mirror is maintained at a constant velocity, the detector will record the signal as a function of time and thus proportional to

the introduced path difference. The interferogram, which is in the time domain, will be converted to a frequency domain spectrum through the application of the Fourier transformation.[1,5] It is essential to determine the exact position of the moveable mirror at all times. This is achieved through the monochromatic radiation of a HeNe laser (632.8 nm), which produces an interference pattern that can be used to measure the position of the moveable mirror with high precision.

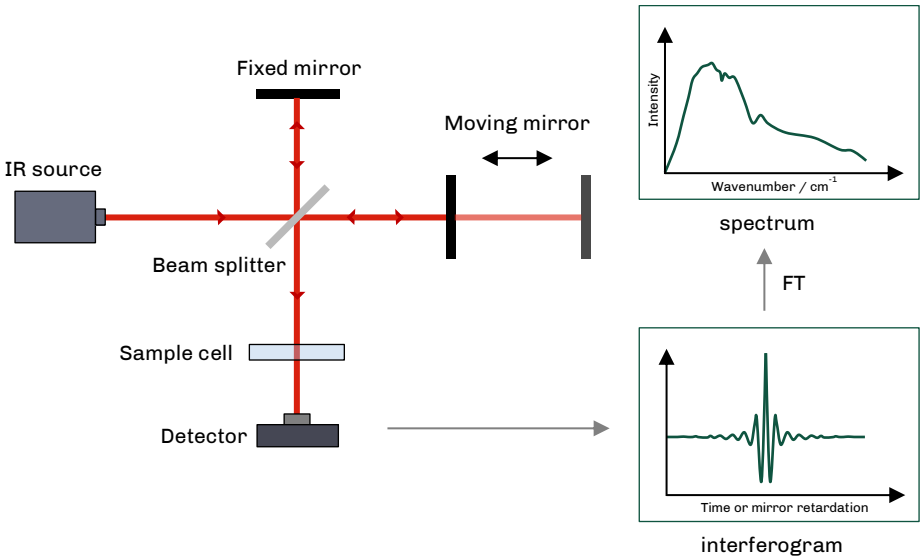

Figure 8: The operating principle of an Michelson interferometer, adapted from Neves, et al. [30]. By moving the mirror, the path difference between the two arms will change and an interference pattern will be recorded depending on the wavelength of the light source.

1.4.2 Laser-based Infrared Spectroscopy

Since its introduction, the Fourier transform technology has significantly contributed to the fast growth and today´s broad availability of infrared spectrometers. The continued development of sources, detectors as well as the expansion of measurement modalities like attenuated total reflection or coupling an FT-IR spectrometer to microscopes has contributed to the growth of a broad variety of different application scenarios for IR spectroscopy. Also enhanced computing capabilities, and optimized data processing techniques have facilitated the successful application of IR spectroscopy to solving a broad range of analytical chemical problems in different field.

Peter Griffiths has identified the invention of quantum cascade lasers (QCL) as the most significant advancement in the field of IR spectrometer instrumentation over the past three decades.[31] Unlike light sources such as the Globar, which adhere to the Planck radiation law, lasers demonstrate high frequency and spatial coherence, resulting in a higher spectral power density. The initial quantum cascade laser was demonstrated by Faist, et al. [32] in

1994. Subsequently, the technology advanced rapidly, and a multitude of prospective applications became evident. The advantages of QCLs include a combination of high power and tunability over a few hundred wavenumbers with room-temperature operation.[33]

In contrast to conventional semiconductor lasers, QCLs do not emit light through the recombination of electrons from the conduction band with holes in the valence band. However, light emission is enabled by inter-subband transitions of electrons within the conduction band, a phenomenon made possible by the heterostructure design of the active region. QCLs are constructed from a multitude of alternating layers, formed from semiconducting material by molecular beam epitaxy or metal–organic vapor phase epitaxy.[33] The superlattice structure is responsible for the formation of several nanometer-thick quantum wells. When an electric field (bias) is applied across the chip, it drives electrons to cascade through a series of quantized energy states within these wells. Each section of the structure is composed of an active region and an injector region, separated by a tunneling barrier. In the active region, electrons are injected into a higher inter-subband state of the conduction band, and as they transition to a lower inter-subband state, a photon is emitted. Subsequently, the electron tunnels through the barrier into the injector region. Since the tunneling process occurs at a much faster rate than the radiative transition, a population inversion in the injector region is maintained. As the electron continues to traverse the superlattice structure, it emits additional photons. A schematic representation of this process is provided in Figure 9. Typically, the cascade comprises between 40 and 100 periods. Consequently, an electron will undergo multiple radiative transmissions, thereby achieving a high power density. Moreover, by meticulously calibrating the thickness of the quantum wells in the active region, the wavelength range within which the laser should operate can be precisely tailored. Currently, wavelengths in the range between 3 and 28.5 µm are possible using the InGaAs/AlInAs heterostructures grown on an InP substrate. [7,33]

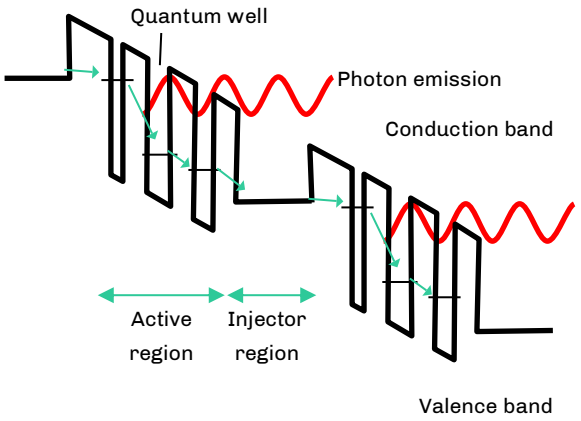

Figure 9: Principle of inter-subband transition and tunneling between the quantum wells of a quantum cascade laser chip, adapted from Quantum Optoelectronics Group [34].

Quantum cascade lasers are classified into three distinct categories based on their resonator design. A QCL with a Fabry-Perot (FP) resonator is characterized by the presence of two high-reflection coatings on the end facets of the chip. The cavity length thus defines the conditions for light amplification, which occurs via constructive interference. However, more than one wavelength is amplified since a number of wavelengths satisfy the standing wave condition. Consequently, the FP configuration yields a broadband laser source, which is only suitable for applications where wavelength tuning is not necessary.[7,35]

A distributed feedback (DFB) QCL with a Bragg grating integrated in the laser waveguide is commonly used for gas phase analysis. This Bragg grating is characterized by the periodic variation of the refractive index, so that only the wavelength that satisfies the Bragg condition is reflected. The DFB-QCL is therefore a single mode laser.[36] However, it can be tuned up to about 5 cm^{-1} wavenumbers by changing the injection current or the operating temperature, which in turn changes the refractive index of the QCL chip. The resonance wavelength shift can be achieved with a tuning rate of about 0.1-0.2 cm^{-1} K^{-1}. A wider tuning range can be achieved by using multiple DFB ridges or by implementing a radial second-order Bragg grating etched into the top cladding of the gain medium, so-called ring-cavity surface emitting (RCSE) QCLs.[7,37]

External cavity quantum cascade lasers, on the other hand, are designed to be tunable broadband IR sources. The laser chip is integrated into an external cavity with an additional collimating lens and a rotating diffraction grating. The facet facing the grating is often coated with an antireflective layer, while the other is coated with a highly reflective layer. Depending on the angle of the diffraction grating, only the selected emission wavelength is diffracted back to the chip. A schematic of this arrangement is shown in Figure 10, using a quasi-Littrow configuration as an example. As a result, a broad emission curve with tunability possible over tens to hundreds of wavenumbers is achieved by superimposing different modes. This makes the EC-QCL especially interesting for liquid-phase IR spectroscopy. The wide spectral coverage in combination with the high spectral power density opens up new application possibilities.[7,38]

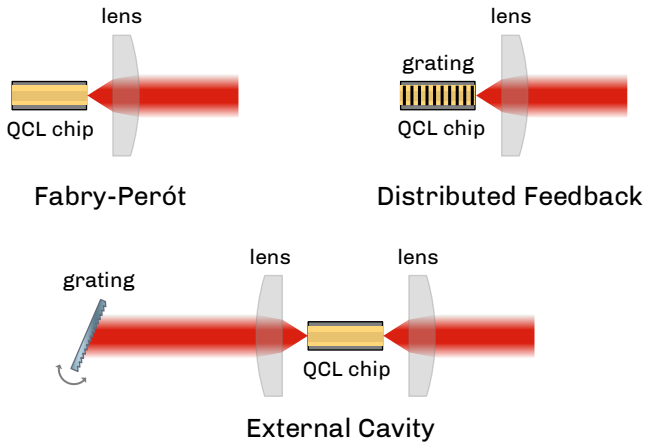

Figure 10: Different types of quantum cascade laser, adapted from Schwaighofer, et al. [7]

1.4.3 M^2 as a Measure of Beam Quality

In laser-based IR spectroscopy and the development of related instrumentation, as demonstrated in this thesis, measuring beam quality is a crucial aspect for ensuring high system performance and overall effectiveness of the equipment. The ideal focused light should normally have a Gaussian (TEM_{00}) shape, minimal divergence, and be diffraction limited. Obviously, this is an unrealistic representation for a real laser, so it is important to characterize the beam. When focusing or expanding a beam, a small initial width helps maintain coherence and minimizes diffraction effects. Several values have been defined to characterize the laser output. First, the Beam Parameter Product (BPP) is the product of its radius at its smallest width, called the beam waist w_0, and the far-field divergence angle θ.[39,40]

$$BPP = \theta w_0 \qquad \text{Equation 11}$$

The BPP has the disadvantage that its value depends on the wavelength of the radiation, making it difficult to compare different lasers. A more common value to describe the beam quality is M^2, which takes the wavelength λ into account. It is desirable to have an M^2 value close to 1, whereas higher values indicate diffraction and distortion.[39,40]

$$M^2 = \frac{\pi \theta w_0}{\lambda} \qquad \text{Equation 12}$$

The M^2 value is calculated according to the ISO 11146-1:202112 standard from the measurement of the beam diameter at a number of different positions. This is achieved by focusing the collimated laser beam with an aberration-free lens. The diameter of the beam

(using the $D4\sigma$ definition) is then measured at different points along the direction of laser light propagation. The focusing lens is used to create an artificial focus. Points very close to the focus (within one Rayleigh length on either side) and points at least two Rayleigh lengths away from the new beam waist are measured. The Rayleigh distance is defined as the distance from the focus at which the beam's diameter is $\sqrt{2}$ times larger than its minimum diameter/radius. Even though the value for the beam waist and the value for the Rayleigh distance z_R will be different, the value for M^2 will be the same as that of the unfocused beam. The beam width can then be plotted against the distance from the lens, a hyperbola is fitted to these points and the values for θ, w_0 and consequently M^2 are obtained. [39,41]

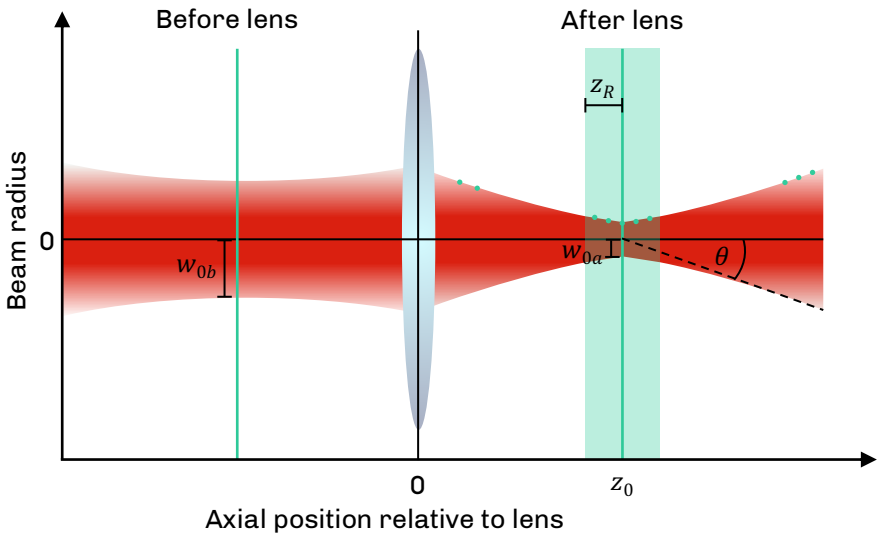

Figure 11: Schematic representation of the positions (green points) at which the diameter of the beam is measured for the M^2 calculations, adapted from Gentec Electro-Optics [39] Instead of measuring the real beam waist w_{0b}, a new beam focus w_{oa} is created with a lens in order to measure within one Rayleigh length z_R and two Rayleigh apart from the focus to properly judge the beam divergence.

1.4.4 Advances in Mid-IR Detector Technology

In modern FT-IR spectrometers as well as laser-based instruments, two principal detector types are employed: pyroelectric and mercury cadmium telluride (MCT) detectors. Pyroelectric detectors like deuterated triglycine sulfate (DTGS) or lithium tantalate detectors employ a thermal detection mechanism, whereby the change in temperature resulting from the absorption of IR radiation is measured. In contrast, MCT detectors utilize a quantum detection approach. The operation of these devices is based on the absorption of photons, which results in the excitation of electrons from the valence band to the conduction band of the semiconducting material leading to a change in the conductivity of

the semiconductor. They are more sensitive and faster than thermal detectors but require cooling usually with liquid nitrogen (77 K) for the operation.[5,7]

A pyroelectric detector operates on the basis of the pyroelectric effect, whereby a pyroelectric material situated between two electrodes undergoes a transient change in electric polarization upon exposure to infrared radiation. One electrode is typically coated with a black material to maximize the absorption of incident light. As the material absorbs infrared radiation and its temperature changes, this induces a shift in polarization, generating a surface charge. The magnitude and direction of this charge are directly proportional to the rate of temperature change, enabling the detection of infrared signals. Since pyroelectric detectors measure the change in radiation and not constant radiation levels, chopping the incident beam is required. The modulation of the infrared signal, typically in frequencies between 10Hz to 100Hz, prevents drift in the detector. [42,43]

In comparison to MCT detectors, pyroelectric detectors are especially regarded for their high linearity and the ability to measure across a broad wavelength range. They exhibit a uniform, wavelength-insensitive response, making them suitable for a range of broad-spectrum applications. In contrast, MCT detectors exhibit a wavelength-specific response with varying sensitivities, which can be fine-tuned by varying the composition of the MCT material, namely the ratio of mercury to cadmium. Additionally, because MCT detectors do not require to change their temperature during the light detection process they are also faster than pyroelectric detectors. However, pyroelectric detectors do not require cryogenic cooling, which results in lower running costs and an overall maintenance advantage over MCT detectors. Given the lower initial cost of a pyroelectric detector, this results in significant economic benefits over MCT detectors.[44,45]

The decision of which detector to choose is often additionally taken based on performance parameters, this includes spectral responsivity and detectivity. Spectral responsivity R_v (V W^{-1}) measures the detectors output V_m (V) per unit of incident radiation power Φ_m (W), providing an efficiency metric:[46]

$$R_v = \frac{V_m}{\phi_m} \qquad \text{Equation 13}$$

The specific detectivity D^* (cm Hz$^{1/2}$ W^{-1}) reflects the detectors ability to distinguish signal from noise, described by the noise equivalent power NEP (see Section 1.3.2):

$$D^* = \frac{\sqrt{A_D}}{NEP} \qquad \text{Equation 14}$$

where A_D is the detector area (cm^2).

Based on the definition of detectivity, the detector area has significant influence, which is especially important for multi-channel detectors, where the individual detector elements are rather small in size.

1.4.5 Multi-Pathlength Transmission Spectroscopy

In transmission spectroscopy, the sample is placed in a transmissive container (i.e., a cuvette, flow cell, or sample holder). The measured absorbance, calculated using the Beer-Lambert law, depends on the concentration and the optical pathlength which is defined by the shape of the container. As discussed in Section 1.3.1, the linear range of the Beer-Lambert law is limited, making it necessary for highly concentrated samples, such as many biological samples, to be diluted to fall in an appropriate absorbance range. However, multiple dilutions can introduce errors and are time-consuming. Alternatively, reducing the optical pathlength would have the same result as dilution but changing the pathlengths of a flow cell can be labor intensive and require some sort of manual skills from the instrument operator.[47] Furthermore, the selection of an optimal pathlength for an IR spectroscopic measurement of analytes in highly absorbing matrices is a challenging task. On the one hand, the use of high pathlengths can result in the total absorption of the radiation in certain spectral regions, leading to the inability to detect a signal at the detector. On the other hand, the utilization of low pathlengths yield in low absorbance values, which in turn can lead to low SNR values. In order to measure the sample at a single pathlength, the highest possible pathlength that allows for throughput at every wavenumber but keeps the absorbance of the sample in the linear range should be selected, which has to be determined empirically in advance. Therefore, instruments and sample holders have been developed that allow absorbance to be measured at different optical pathlengths, without the need of removing the sample from the sample compartment.

A commercial instrument employing variable pathlengths in the UV-Vis spectral region is the SoloVPE by Repligen (Waltham, USA). It features a mechanism that dynamically adjusts the optical pathlength depending on the absorbance by moving a fiber optic probe in the vertical direction within the sample holder. Consequently, the measurement of highly concentrated samples can be conducted directly, without the need for dilution. The instrument has a variety of applications, including the determination of monoclonal antibodies and the testing of gold particles.[48] However, the movement of the fiber probe can cause instability in light intensity, affecting accuracy, particularly for low absorbance samples. The principle of this instrument relies on the linear movement of the probe performed by a motor. These mechanical components introduce a further source of noise and inaccuracy due to friction, thermal expansion, and motor-related errors.[47] Additionally, the SoloVPE operates in the UV-Vis range and translating this technique to the IR spectral range would be difficult due to material limitation.

A wedge-shaped transmission cell used in IR spectroscopy was first described 1971 by Robertson and Williams [49] which they achieved by placing a 20 µm spacer on one side between two CaF_2 windows and sealing the edges with neoprene stripes. The angle of the wedge was determined by observing the interference fringes with a visible light source and the cell was placed on a moveable stage to measure the cell at different pathlengths in succession. This was done in order to accurately measure the absorption coefficient of water. A similar cell was used by Tyler, et al. [50] who used a stainless steel shim stock as spacer and the liquids were only held by surface tension between the windows for easier handling. A shim stock of adequate thickness could be used and changed according to the absorptivity of the liquid. This design was further developed by Wieliczka, et al. [51] who designed an improved holder that did not require disassembly for liquid filling following pathlength calibration with interference fringes. However, all of these wedge-shaped transmission cell designs have the disadvantage of having to be reassembled for each new sample, resulting in small variations in pathlength due to the new alignment. Furthermore, the setups allow for the analysis of a limited range of pathlengths of only approximately 20 µm, which cannot be measured simultaneously.

To overcome the constraint of measuring at a single pathlength, a custom-designed wedged-shaped transmission flow cell is proposed and used in this work to enable simultaneous measurements at multiple pathlengths. The wedge is carved into one of the CaF_2 windows and the inlet and outlet of the flow cell are positioned on the opposite window. The use of a flow system facilitates continuous operation without the need for disassembling the cell, leading to more efficient handling. Additionally, the presented setup allows for the analysis of a significantly broad range of pathlengths (approximately 400 µm). The detailed design and characteristics of the cell will be described in the experimental section of this thesis.

2 Experimental

2.1 Experimental Setup

The experiments were conducted with a quantum cascade laser-based spectroscopic setup that employed a multi-pathlength transmission cell, as illustrated in Figure 12. As a source of IR radiation, an external cavity quantum cascade laser manufactured by DRS Daylight Solutions Inc. (San Diego, USA) was employed, with tunability in the range 1805–1565 cm^{-1} (5.54–6.39 µm). The laser was cooled thermoelectrically and could be operated in either a pulsed or continuous wave mode. In this work, the laser was operated in pulsed mode with a pulse width of 500 ns and a frequency of 100 kHz (5% duty cycle). In order to measure the concentration of bovine serum albumin (BSA) in aqueous solution, it was necessary to change the laser head to another model, which covered the spectral range of 1798–1488 cm^{-1} (5.56–6.72 µm).

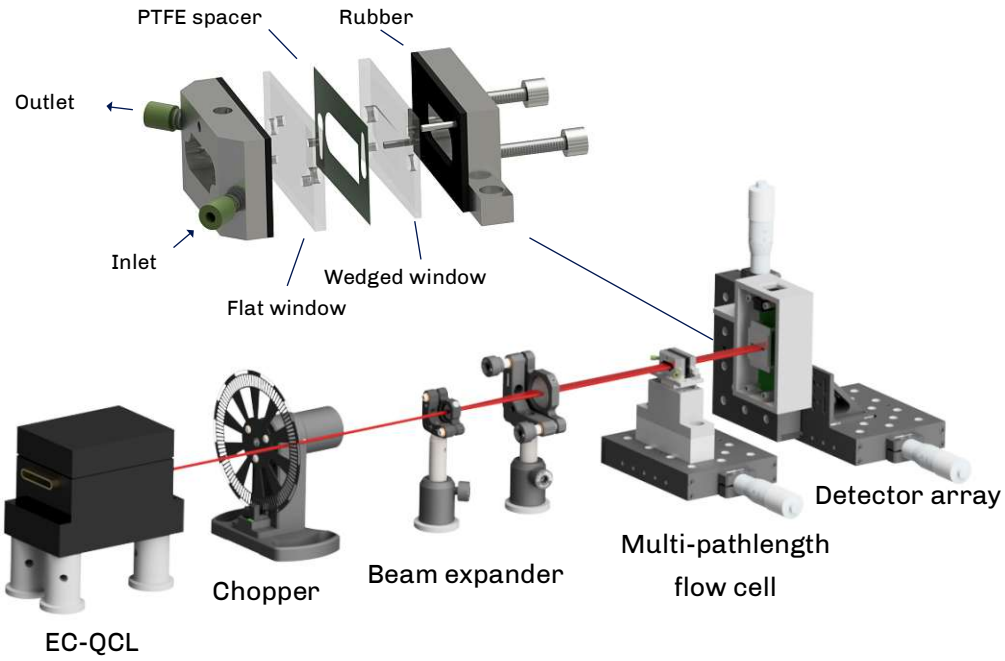

Figure 12: Design of the multi-pathlength QCL-based setup in which the beam is expanded to a line with cylindrical lenses and the signal is detected via a pyroelectric array detector. The flow cell is equipped with a wedge-shaped window (top).

The laser and its associated parameters, including power, wavelength, temperature, scan speed, and pulse parameters, were controlled by a low-noise laser controller (DRS Daylight Solutions Inc., San Diego, USA) and operated with a Python script over the software development kit (SDK) provided by the supplier. The beam width was measured with a

laser beam profiler (Pyrocam™ III HR, Ophir Optronics Solutions Ltd., Jerusalem, Israel) and the laser power was determined by a power meter (PM160T, Thorlabs Inc., Newton, USA).

The laser beam intensity was further modulated by an optical chopper (MC2000B, Thorlabs Inc., Newton, USA), the frequency of which also determined the readout frequency of the detector. The detector (256LTI SP0.5, Dias Infrared GmbH, Dresden, Germany), placed approximately 43 cm from the laser, consisted of a pyroelectric linear array containing 256 sensitive lithium tantalum elements and an evaluation kit, which generated the required clock pulses and transformed the signal output into a digital format. The dimension of each sensitive element was 42 µm by 500 µm (pitch 50 µm) in front of which an 0.5 mm thick anti-reflective (2.5 - 14 µm) coated Germanium window was installed for protection. The detector was supplied with electricity by a Dual Output DC power supply (E3620A, Agilent Technologies Inc., Santa Clara, USA), which ensured low noise and a stable power output. The system was either controlled via the GUI or by integration of the evaluation kit in a Python script.

The Gaussian laser beam is expanded by two plano-convex, round, cylindrical CaF_2 lenses (LJ5386RM and LJ5654RM, Thorlabs Inc., Newton, USA), which are aligned in a Keplerian beam expander configuration. The resulting collimated laser line then passes through a custom-made liquid flow cell, milled from aluminum, which is constructed from two CaF_2 windows (Crystran Ltd, Poole, UK) separated by a PTFE spacer with a thickness of 6–12 µm. A wedge is carved into one of the windows, thereby creating increasing pathlengths across the window area. At the widest point of the cell, the pathlength is 430 µm longer than at the opposite end, where it is defined by the spacer thickness. The flow cell is thermoelectrically stabilized at 25 °C by a Peltier element and a temperature NTC sensor, which is controlled via a TEC controller (Meerstetter Engineering GmbH, Rubigen, Switzerland). The cell was first designed on a design-extension application Inventor (Autodesk Inc., San Francisco, USA) for which the technical drawings can be found in the Appendix of this thesis.

The cell and detector are mounted on moveable stages to facilitate optimal alignment. The entire system is enclosed in a housing and flushed with dry air before and during the measurements to minimize the impact of water vapor on the recorded spectra. The dry air was supplied to the system via several pneumatic silencers connected in series to diffuse the exhaust dry air. The housing was constructed from acrylic glass and coated with a black adhesive film to minimize the impact of stray light on the detector.

2.2 Data Acquisition and Post-processing

Data acquisition during the measurements was controlled by a Python script which first sets the given parameter for the detector and laser. Three dark scans (laser off) were recorded before and after each measurement. This was done to account for the zero offset of the detector, which was approximately 2.5 V. A step wise acquisition mode of the laser was then used to record the spectrum (step size between 0.1 and 0.5 cm^{-1} with a duration of approximately 0.5 s per step). The recorded signal from the pyroelectric detector and the detector temperature were stored in a text file at the end of each scan for further processing. For each measurement series, at least three background (solvent) measurements were recorded, and each sample was then measured three times. After ensuring that the recorded results were usable (by checking for non-zero data, and the absence of anomalies due to air bubbles, etc.), the first step of post-processing was to average the three background scans. Since each detector element recorded a scan corresponding to a different optical pathlength of the sample solution, the results were filtered by removing the portions of each scan where the detector was oversaturated or showed no signal due to total absorption. This was done for both the sample scans and the averaged background scans.

The absorbance spectrum for each pathlength (detector element) was then calculated based on the Beer-Lambert law and the absorbance spectra from the three repeated measurements were averaged. The calculated spectra were then normalized by the pathlength corresponding to each detector element, so that the height of the absorbance bands was dependent only on the concentration of the solution. This resulted in a spectrum for each detector element, which were then combined based on a weighted average depending on the pathlength-to-noise ratio (for further details see Section 3.3). The final spectrum for each sample was therefore the combination of several scans at different pathlengths.

2.3 Chemicals

The chemicals utilized were of analytical grade and procured from Sigma-Aldrich (Steinheim, Germany). For the different measurements, (i) solutions of caffeine in ethanol (≥99.8%), (ii) caffeine in deionized water and (iii) bovine serum albumin (BSA) in deionized water were prepared. Dilution series were prepared in volumetric flasks with concentrations ranging from 2.5 to 25 mM for caffeine in ethanol, 5 to 25 mM for caffeine in deionized water and 1 to 50 mg mL^{-1} for BSA in deionized water.

2.4 Reference with FT-IR

The objective of the FT-IR measurements was to compare the performance of the self-constructed setup with that of a conventional high-performing research-grade spectrometer. Additionally, to assist in calibrating the pathlengths of the wedged-shaped transmission

cell, measurements of caffeine in ethanol dilutions were made with an FT-IR transmission flow cell with four different pathlengths.

The measurements were conducted on a Bruker Vertex 80v FT-IR spectrometer (Bruker, Ettlingen, Germany) in transmission mode with a flow cell featuring pathlengths between 6 and 104 µm mounted in the sample compartment, which was maintained under constant flushing with dry air. The fringing effect was employed to determine the precise thickness of the sample cell. The resolution was set to 4 cm^{-1} with an aperture size of 4 mm. A total of 64 scans were recorded and averaged for each spectrum (scan time 100 s), which were then processed using the Bruker OPUS software.

3 Results and Discussion

In the following chapter the setup, described in Chapter 2, and its development is discussed in more detail. The multi-pathlength spectroscopy setup was assembled from scratch. The quantum cascade laser was evaluated for beam quality and power consistency. Two different versions of custom beam expanders were built and tested for beam shape and intensity uniformity. The array detector was characterized, and optimal operating parameters were determined. Furthermore, the performance of the setup was validated through preliminary measurements of an analyte in an evenly absorbing solvent. Finally, aqueous solutions were measured, a method for the pathlength selection was developed, and the final protein measurements were demonstrated using BSA as an example.

3.1 Setup Development Process and Characterization of Components

In the development of an experimental setup, defining and assessing the characteristics of each component is crucial. This meticulous process not only ensures optimal performance but also helps in identifying sources of noise that can impact the accuracy of measurements. This chapter details the setup development process, describes the characterization of key components, and explains the steps taken to optimize performance and reduce noise.

3.1.1 Verification of the Laser Performance

The development of the setup began with the characterization of the radiation source, including the determination of the beam width and the beam quality M^2. A quantum cascade laser with tunable wavelengths between 1805 and 1565 cm^{-1} was utilized in the initial stage of the setup. According to the supplier, the output beam exhibits a diffraction-limited Gaussian profile with a beam quality M^2 value below 1.2 with the beam waist being situated approximately 30–50 cm from the exit port.[52]

To verify that the laser operates within its specification, the incident power on the detector was measured at various wavelengths, as shown in Figure 13A. According to the supplier, the maximum average output power of the laser operated in a pulsed mode (100 kHz, 500 ns) at a maximum laser current of 650 mA is 34.5 mW at 1693 cm^{-1}. The same test conditions were used for the validation measurement, where the power was measured every 5 cm^{-1} with a power meter. The resulting power curve was comparable to the data sheet, and a maximum power of 33.8 mW was measured at 1695 cm^{-1}. The effect of radiation absorption by water vapor in the air can be seen in the measurement with a significant decrease in spectral power reaching the detector at 1655 cm^{-1}. The implication of the wavenumber dependent output power is that the expected noise will be higher at these

wavenumbers which correlate with lower output power, as higher output power correlates with lower noise.

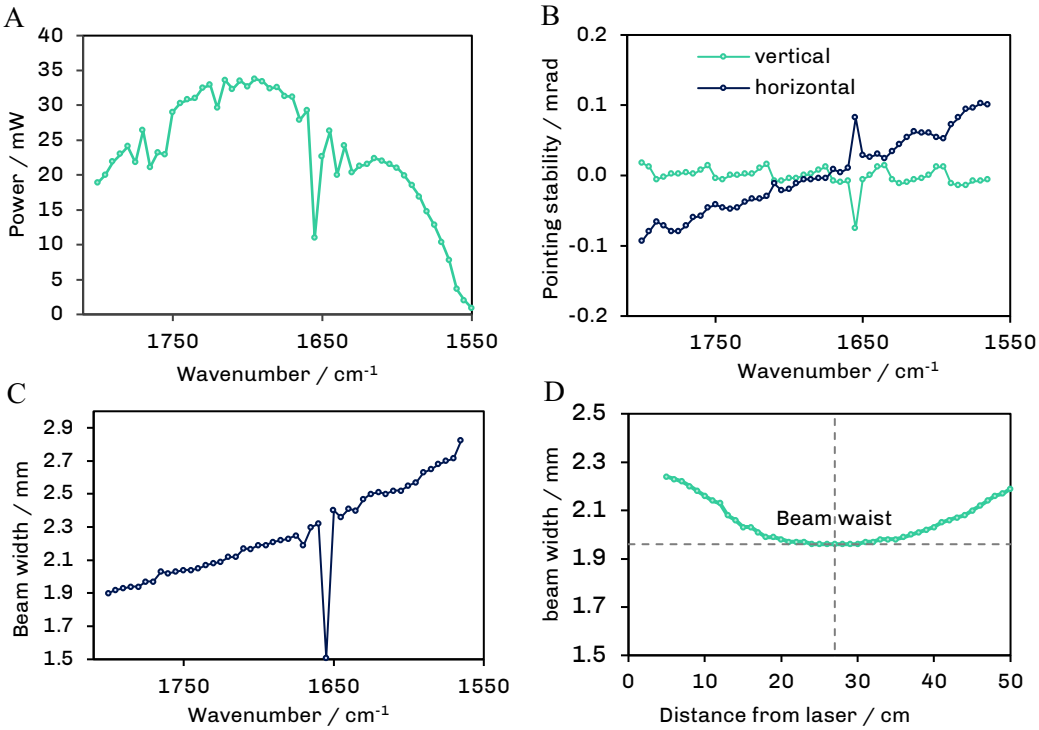

Figure 13: Characterization of the laser performance. The maximum power of the laser was 33.8 mW at 1695 cm^{-1} (A). A very good pointing stability with the deviation being under 0.2 mrad was observed for both vertical and horizontal beam position (B). The beam width was dependent on the wavenumber (C) and the distance from the exit port of the laser with the beam waist positioned at 27 cm distance from the laser (D).

Additional validation of the behavior of the lasers over the covered wavenumber range was performed on the pointing stability (i.e., whether the position of the laser beam moves during tuning). The pointing stability was evaluated using a laser beam profiler located at a distance of 50 cm from the laser exit port. The laser current had to be reduced to 450 mA to avoid oversaturation of the beam profiler. The results in Figure 13B show that the sample used for this experiment has a very high pointing stability with a maximum deviation from the center of 0.2 mrad in the horizontal direction and 0.1 mrad in the vertical direction. A periodic pattern of the pointing stability can also be observed. This is caused by the movement of the grating of the external cavity QCL. At 1655 cm^{-1}, the deviation of the beam from the center seems to be more significant, which can be explained by the lower power due to radiation absorption by water vapor. This reduction in power also resulted in a smaller beam diameter, making it difficult for the laser beam profiler to measure accurately, thereby introducing greater uncertainty into the measurement at this wavenumber. A high pointing stability is especially important in the case of this experiment

because the setup uses a beam expander that is very sensitive to movement of the laser beam, as a laser beam entering the beam expander off-center would result in an amplified deviation when hitting the detector. Overall, these tests demonstrated the high pointing stability of the laser showing that the model is well suited to be used in this experimental setup.

Similar to the pointing stability, the beam width was also measured with a laser beam profiler at the same settings. This was done to ensure that the laser was operating within specification and did not deviate largely from a beam width of 2.5 µm ($1/e^2$). The beam width should be kept as small as possible for subsequent expansion and to minimize spherical aberration. Two different approaches on measuring the beam width were taken. In the first measurement (Figure 13C), the beam width was measured at every 5 cm^{-1} at a constant distance of 50 cm from the laser. In the second measurement (Figure 13D), the wavenumber was kept constant at 1695 cm^{-1} but the distance to the laser was varied between 5 and 50 cm. These measurements were used to locate the beam waist, which was then used to optimally position the beam expander within the experimental setup at a distance of 27 cm.

Lastly, the beam quality parameter M^2 was evaluated in accordance with the ISO 11146-1:202112 standard, using the laser beam profiler and a plano-convex lens to meet the required spatial constraints. To prevent spherical aberrations, it is necessary to ensure that the lens has a f-number, defined as the focal length divided by the beam diameter, that is greater than 20.[53] Accordingly, a lens with a focal length of 200 mm was selected, resulting in an f-number of approximately 100. The measurements were conducted at a wavenumber of 1695 cm^{-1}, with a laser current of 400 mA. The beam quality calculations were performed using a Python script developed by Prahl [53] The results illustrated in Figure 14, demonstrate that the laser beam exhibits an exceptionally high degree of quality, with a beam quality parameter M^2 of 1.03 ± 0.01, which is in close agreement with the ideal beam quality of 1.

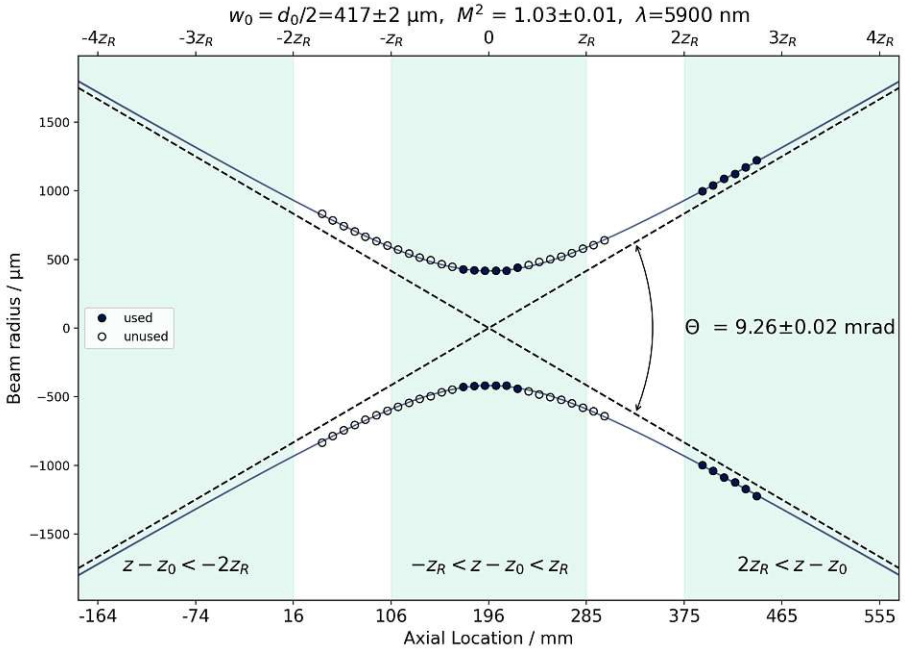

Figure 14: Beam quality M^2 was calculated by measuring the diameter of the beam at five points within a Rayleigh length z_R and at five points at least two Rayleigh lengths distant from the artificial beam waist (dark blue points). Points measured but not used for the calculation are marked without filling.

3.1.2 Characterization of the Detector Parameters

After the laser performance has been validated the detector parameters had to be characterized. The pyroelectric linear detector used in this experimental setup consisted of 256 detector elements which in total cover a distance of 12.8 mm and had a Germanium window in front of the detector array with a thickness of 0.5 mm. According to the specification sheet, the modulation frequency of the detector elements can reach up to 512 Hz, however it is further limited by the control electronics, which can only operate within a range of 10-100 Hz. According to the supplier, the detector has a mean noise voltage of 0.94 mV and a responsivity of 537 kV W^{-1}.

The electrical diagram for the detector's internal read out circuit is given in Figure 15. The circuit is optimized for low noise and high linearity consisting of an analogue and a digital part of which only the analogue path is shown below for simplicity. The pyroelectric elements are operated in current mode, which means the charge generated by the pyroelectric elements are first converted to a current for further processing. The signal is then integrated, therefore accumulating the current over a specific time (integration time) to produce a voltage that represents the detector signal. The signal is then stored in a sample & hold stage, in which the signal is hold until the multiplexer sequentially switches these

channels to the output drive. The signal of each detector element is read one at a time, contributing therefore to the higher sampling times compared to single channel pyroelectric detectors.

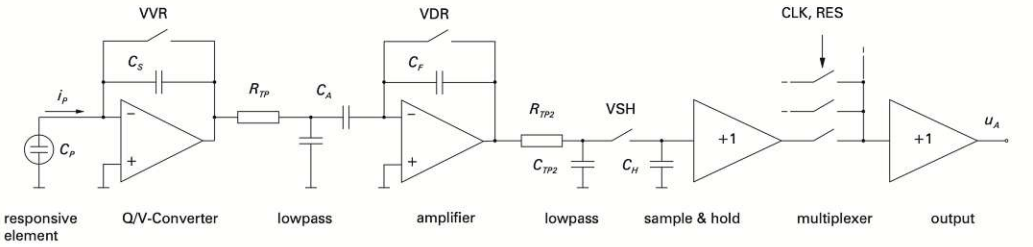

Figure 15: Internal readout circuit of the detector. [54]

The most relevant detector parameters that need to be set for the experiment are the readout frequency, the duration of the variable voltage regulation (VVR) and the voltage dependent resistor (VDR), the integration time, and the lowpass settling time. These parameters are related in the following way:

$$Modulation\ time = VDR + integration\ time \qquad \text{Equation 15}$$

$$VDR = VVR + lowpass\ settling\ time \qquad \text{Equation 16}$$

VVR and VDR are digital inputs, which control the analog preset but which functions are not stated further by the supplier. For all the subsequent measurements, the VVR time t_{VVR} was set to 30 µs, as per the manufacturer's recommendation. The modulation time, and thus the readout frequency, was set to 64 Hz. The integration time was configured to 8.900 ms, as this yielded the highest signal at the set readout frequency. Based on these settings and their correlations, the lowpass settling time was calculated to be 6.695 ms.

To characterize the detector's performance parameters, it was positioned in front of the laser at the distance of the beam waist. Additionally, the chopper's frequency output was given to the detector as a trigger impulse to determine and synchronize its read-out frequency. The first characterization of the detector involved the measurement of the detectors dark noise. The laser was therefore turned off and over 370 acquisitions (each were recorded with the settings described above) were conducted. A mean dark noise of 1.93 mV was determined with higher noise voltages on the right side of the detector (see Figure 16). One reason for this could be that the signal of these detector elements is stored longer at the sample & hold stage before being collected by the multiplexer.

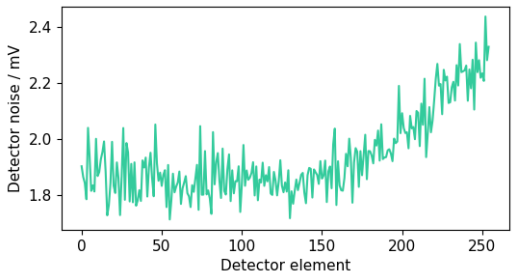

Figure 16: Dark noise of the detector for each detector element.

The stability of the detector over time was then analyzed by measuring the detector output signal with a constant incident laser power at 1695 cm^{-1} over a duration of 80 minutes. The measurement was started in the morning, to assess a possible acclimatization phase in which the detector was still warming up. The results are presented in Figure 17 for which two measurements were conducted: one with and one without the purge of dry air during the measurement. The measurement conducted at ambient environment showed higher outlier than the one which was flushed with dry air. Additionally, the temperature was measured for the second measurement with dry air since a significant overshoot was recorded for both measurements due to temperature differences. It was therefore decided to let the detector run at least for 25 minutes before starting any measurements.

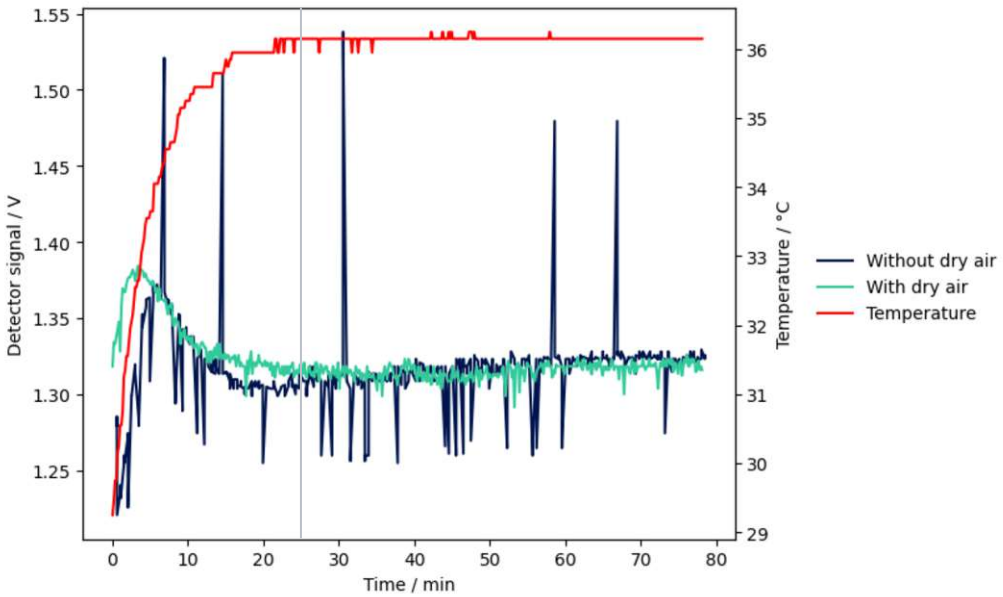

Figure 17: Detector performance over time before and after the installation of a housing and a dry air supply. The temperature measurement was conducted at the measurement with dry air and shows a warm-up phase of the detector of 25 minutes.

As stated above, the detector has a readout frequency of 10-100 Hz. However, it was noticed when tuning the laser in the step-and-measure mode that when the signal was

recorded directly after the tuning, a slight overshoot or undershoot was measured. Therefore, a time function was built into the acquisition code which started the recording of the signal not until 0.4 s after the tuning occurs and the detector had time to adjust to the new radiation. Each scan (recording of all 265 detector elements) took consequently about 0.5 s, which in case a wavenumber range of 250 cm^{-1} is covered at a scan rate of 0.5 $cm^{-1} s^{-1}$ sums up to approximately 5 minutes per measurement including the dark scan measurement and saving of the data.

3.1.3 Development of a Beam Expander

Following the validation measurements for the laser and the detector, the beam expander was developed. The beam expander was employed to reshape the laser beam into a line that would subsequently pass through the wedged-shaped transmission cell. In addition to altering the beam's shape, the expander's purpose is to ensure a uniform distribution of laser beam intensity across the newly formed shape. This is crucial for achieving comparable results across the detector. To achieve this behavior, specialized commercial products are available, such as the Powell lens, which creates straight, uniform laser lines by fanning out collimated beams in one dimension. This lens has the property of reshaping the beam into a near-complete flat-top profile, which is desirable for the purposes of this experiment. Nevertheless, there is currently no Powell lens commercially available that is suitable for use in the IR spectral region. Other options, such as the π-Shaper (Edmund Optics Inc., Barrington, USA), were designed to ensure a uniform intensity distribution and a flat phase front but were also only available for the UV-Vis region. Accordingly, the decision was taken to expand the beam in a single dimension to create a line with a Gaussian intensity profile. Subsequently, the beam could be reshaped into a beam with a flat-top intensity profile by means of an aspherical apodization filter. The apodizer functions by selectively attenuating the central area of the beam to a greater extent than the edges, thereby resulting in a more uniform intensity distribution. However, in the course of this research, the initial setup was developed and tested without an apodizer to confirm its functionality first and establish proof-of-concept. As detailed later in this work, satisfactory results were achieved. Nonetheless, the incorporation of an apodization filter may be advisable for future improvements.

The initial design included a beam expander in the configuration of a Galilean telescope, utilizing one convex and one concave cylindrical mirror. The decision to employ a mirror-based design for the beam expander was based on the understanding that reflective beam expanders exhibit reduced chromatic aberration and, consequently, superior optical performance compared to lens-based designs.[55] However, given the difficulty in obtaining the concave cylindrical mirror (polished, metal-coated) to combine with the convex mirrors, I undertook the task of fabricating the required mirrors myself. This was achieved through the sputter deposition of gold on specially cut glass tubes. A sputtering rate of

500 s at 30 mA at 7 cm distance between the substrate and the target resulted in the most uniform coating of the thin film, with a thickness of approximately 150 nm. The resulting optical mirrors were then mounted and positioned at the specified angles and distances relative to one another, according to the specifications of the Galilean design, in order to achieve the desired degree of beam expansion, as illustrated in Figure 18. The anticipated beam expansion m_{12} for this configuration is 4.75 (see Equation 17). The convex mirror had a radius of 10 mm and a focal length f_1 of 5 mm, while the concave mirror had a radius of 47.5 mm and a focal length f_2 of 23.75 mm. In this configuration, the initial convex mirror expanded the beam, while the subsequent concave mirror collimates it to the desired final beam expansion width.

$$m_{12} = \frac{f_2}{f_1} = 4.75 \qquad \text{Equation 17}$$

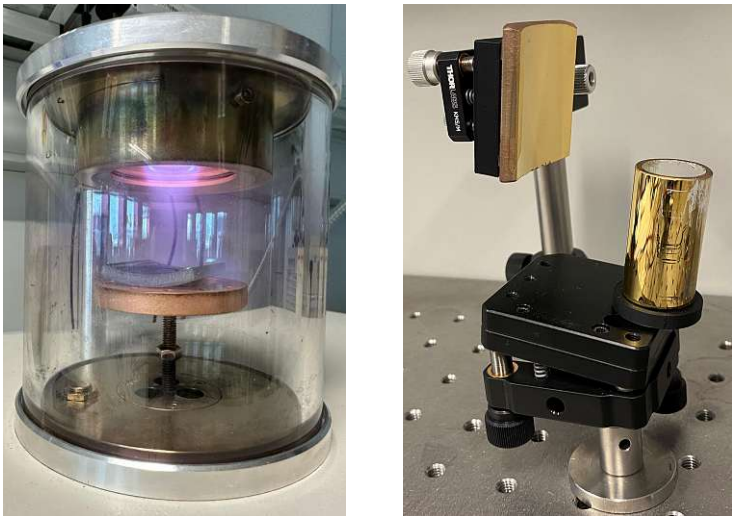

Figure 18: The sputter process was employed to coat the cylindrical-shaped glass pieces with gold (left). The resulting beam expander (right). The mirrors were mounted at an angled orientation, enabling the beam to pass over the initial mirror following its reflection and collimation by the second.

The quality of the beam expander was evaluated through the utilization of a beam profiler mounted on rails, which recorded the shape of the resulting beam at distances between 5 cm and 29 cm from the second mirror. This was done to determine whether the beam, after passing through the expander, retains the desired shape along the entire distance to the detector. The measurements were performed at a laser current of 650 mA and a wavelength of 1695 cm^{-1}. The results are presented in Figure 19.

The images captured by the beam profiler indicate that the beam was expanded to a linear shape with a horizontal beam width of 8.01 mm while maintaining a vertical beam width of 2.00 mm, which is adequate to cover 160 of the 256 detector elements. However, a

significant attribute of the resulting beam is not only the covered area and linear expansion, but also the uniform Gaussian distribution of beam intensity. It is unfortunate that the results are not satisfactory in this regard, as the beam shape in the expanded horizontal direction deviates from the Gaussian intensity distribution. As can be observed in the images in Figure 19, the intensity maximum moves off center when moving away from the expander.

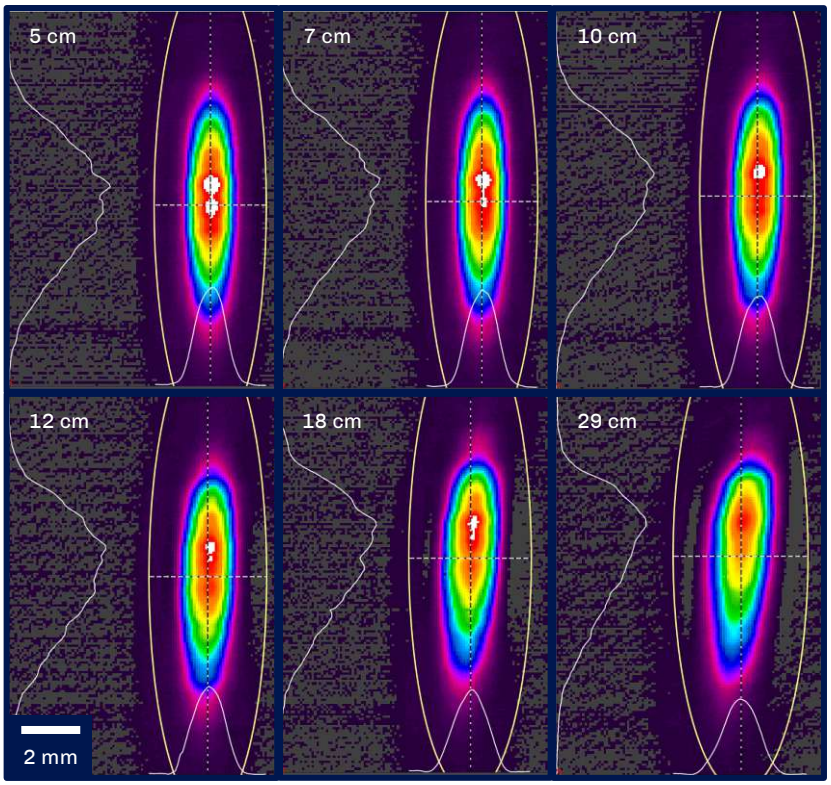

Figure 19: Shape of the laser beam expanded with the gold-coated mirrors analyzed at distances between 5 cm and 29 cm from the second mirror.

The poor performance of this beam expander setup is likely to be explained by the insufficient optical quality of the mirrors. The glass tubes used in the mirror fabrication process were not of optical grade, which may have resulted in a higher textured surface, potentially leading to the scrambling of the wavefronts. During the development of the sputtering process, flat glass pieces were coated with gold to assess the thickness and the roughness of the thin film. For the parameters which were used in the end for the coating of the glass tubes, a surface roughness of approximately 30 mA was recorded with a profilometer (DektakXT, Bruker, Ettlingen, Germany). This aligns with the maximal roughness for optical mirrors according to the Rayleigh roughness criterion.[56] However, it was not possible to measure the cylindrical glass tubes with the profilometer as only flat surfaces can be analyzed. The potential error lies therefore potentially in the roughness and waviness of the glass tubes.

Due to these results, it was decided that this beam expander setup will not be used in the forthcoming experiments. An even intensity distribution is of particular significance in this experimental setup, as the incident intensity on the individual detector elements must be clearly defined to facilitate the appropriate interpretation of the results. This is because the different detector elements correspond to different cell pathlengths, necessitating the interpretation of each element individually.

Therefore, an alternative beam expander setup was built based on a design utilizing lenses. The lens-based design was chosen to eliminate the uncertainty around in-house made optical components as lenses that are suitable for the use within the IR region are commercially available. Two CaF_2 convex lenses were acquired and assembled in a Keplerian beam expander design. The challenge with the Keplerian design lies in the high optical standards required from the optical components as wavefront scrambling and spherical aberration is more likely due to the specific arrangement of the elements, these requirements were taken into consideration when procuring the lenses. Furthermore, wave front errors could occur with this design due to the heat caused in the air between lenses if high power lasers are used, which we could not observe as the laser power in our setup is not high enough for this phenomenon to occur.

In this configuration, the first lens had a focal length f_{l1} of 20 mm and the second lens had a focal length f_{l2} of 100 mm. This yields an expansion coefficient m_{l12} of 5, which should result in a beam width of approximately 1 cm.

$$m_{l12} = \frac{f_{l2}}{f_{l1}} = 5 \qquad \text{Equation 18}$$

To confirm the characteristics of the resulting beam, a beam profiler was utilized in the same configuration as with the mirror-based expander previously employed. The intensity distribution of the resulting beam was recorded at varying distances from the expander, extending from 1 cm to 35 cm in this instance. The measurements were performed at a laser current of 575 mA and a wavelength of 1695 cm^{-1}. As illustrated in Figure 20, the resulting beam from the lens-based setup exhibits a Gaussian intensity distribution, which is particularly evident when comparing the results to those obtained with the mirror-based beam expander. The beam width as determined by the beam profiler was 8.64 mm in the horizontal direction and 2.00 mm in the vertical direction. As the distance increases, a slight decline in intensity is observed. This can be attributed to the absorption of radiation by water vapor and a minor divergence, which, however, does not present a concern for this particular application and is in line with the anticipated behavior. The results of these tests demonstrate that the lens-based beam expander performs satisfactorily and was therefore used for the remainder of this work within the setup.

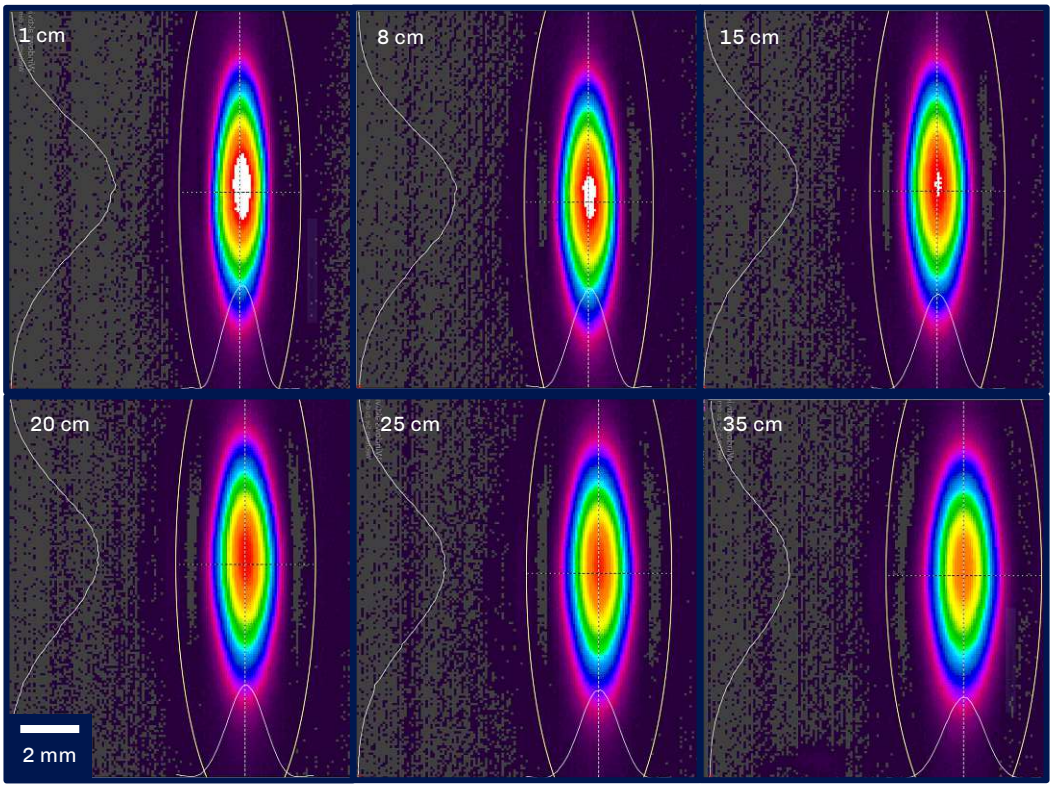

Figure 20: Shape of the laser beam expanded with the plano-convex lenses analyzed at distances between 1 cm and 35 cm from the second lens of the beam expanding configuration.

3.2 Preliminary Measurements and Pathlength Calibration – Ethanol as a Uniform Absorbing Matrix

Subsequent to the assessment of the laser and the detector's operational capabilities, a series of preliminary tests were conducted on solutions of caffeine in ethanol. Ethanol was utilized as the solvent, as it exhibits minimal absorbance in the mid-IR region between 2800 and 1500 cm^{-1}. Caffeine was selected as the test substrate due to its two distinct absorbance bands (corresponding to the C=O stretching vibrations) within the wavenumber range of the detector, its availability, and its solubility in both water and ethanol. Prior to the incorporation of the beam expander and the multi-pathlength transmission cell, the functionality of the setup - which consisted of the laser, chopper, detector, and a flow cell with a constant pathlength of 104 µm - was examined through the assessment of the absorbance spectrum (see Section 3.2.1). Subsequently, the beam expander was installed, and the test solutions were measured again with the improved settings (see Section 3.2.2). By measuring the absorbance of the caffeine solutions with flow cells of different pathlengths, a calibration set was generated for the following installation of the multi-pathlength transmission cell. With the absorbance data from the measured known pathlengths, it was possible to determine which detector element corresponds to which part of the wedged-shaped transmission cell (see Section 3.2.3 for more detail).

3.2.1 Optimization Process of the Setup without Beam Expander

A flow cell with a constant pathlength of 102 µm was mounted in front of the array detector for the first measurements of samples. The cell thickness was determined with the interference fringe method. A FT-IR spectrum with the empty cell in the beam path was therefore recorded beforehand and the fringes, resulting from the reflection of radiation from the parallel windows and interference with the incident beam, were counted. The pathlength could then be calculated with the following equation:

$$d = \frac{10000\, n}{2(\tilde{\nu}_1 - \tilde{\nu}_2)} \qquad \text{Equation 19}$$

where d is the pathlength (µm), n represents the number of fringes, and $\tilde{\nu}_1$ and $\tilde{\nu}_2$ are the starting and ending wavenumber (cm^{-1}).

As preliminary test substance, caffeine with a molarity of 25.7 mM in ethanol, was utilized in the initial measurements, which were conducted following the connection of the optical chopper with the detector (see Section 3.1.2). The measurements were conducted with a laser power of 295 mA, a modulation frequency of 10 Hz, an integration time of 68 ms and a step size of 1 cm^{-1}. However, the absorbance bands of caffeine are obscured by high noise levels, as illustrated in Figure 21A. Accordingly, a number of modifications were implemented with respect to the settings and the system. An acrylic glass housing was constructed, incorporating openings for cables, tubing, and a dry air supply, which was introduced into the setup via a tube. Subsequently, alterations were made to the laser and detector settings following an empirical assessment of the noise at varying adjustments to a laser power of 305 mA, a modulation frequency of 64 Hz, and an integration time of 8.9 ms (see Figure 21B). Further noise reduction could be achieved by coating the housing with a black adhesive film and installing several pneumatic silencers to the dry air supply to diffuse the exhaust dry air. Furthermore, the detector was connected to a stable DC power supply, which ensured lower detector noise and a stable power output. While the other settings of the components were maintained, the step size of the tuning was reduced to 0.1 cm^{-1} (see Figure 21C). Despite the presence of a few outliers in the spectrum, which were attributed to inaccurate modulation pulses sent from the chopper to the detector, these configurations yielded satisfactory results, as these could be removed in the post-processing stage. Consequently, it was decided to proceed with these settings and install the beam expander as the next step.

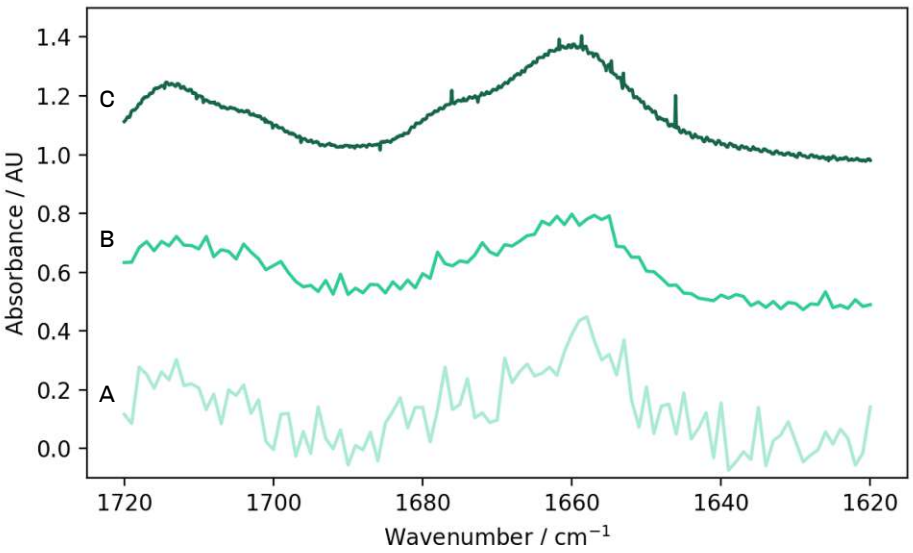

Figure 21: Evolution of the setup based on the absorbance measurement of caffeine in ethanol. The improvements of the laser and detector settings as well as the installation of a housing with a dry air supply led to a substantial reduction of noise. This is visible when comparing the first spectrum recorded with 10 Hz modulation time and ambient humidity (A) to a spectrum recorded with a modulation time of 64 Hz and dry air supply (B) and to one taken with an improved housing and after the installation of pneumatic silencers (C).

3.2.2 Introduction of the Beam Expanding Lenses

As detailed in Section 3.1.3, the beam-expanding optical components were mounted into the setup. The initial design employed two self-fabricated mirrors, as no commercially available alternative was found. However, due to the inferior performance of the mirrors, they were replaced by a set of cylindrical lenses mounted in the Keplerian telescope design. Prior to this, the unequal intensity distribution of the reflective beam expander design was recorded by the detector, as illustrated in Figure 22. In contrast, the transmissive beam-expanding optics led to a symmetric intensity distribution, as verified by the beam profiler. However, despite the beam appearing as a Gaussian profile on the beam profiler, the shape of the beam detected by the detector array was found to be relatively flat-top shaped with a distinct interference pattern. The fringes were clearly discernible in both the shape of the beam (see Figure 22) and in the recorded scans across the wavenumbers. Accordingly, the interference fringe method was employed to ascertain the distance between the two parallel reflective surfaces that were responsible for generating the interference pattern. The calculations indicated that the length was approximately 500 µm, which is consistent with the thickness of the protective germanium window situated in front of the pyroelectric detector elements. Despite the window having an AR coating, the interference fringes, caused by the high refractive index differences between the window and the adjacent medium, are very pronounced. Unfortunately, the removal of the window was not possible without the possibility of damaging the detector. It was therefore decided that the

measurements would be carried out with this setup, as it was still possible to demonstrate the concept as a potential solution for measuring unevenly absorbing matrices.

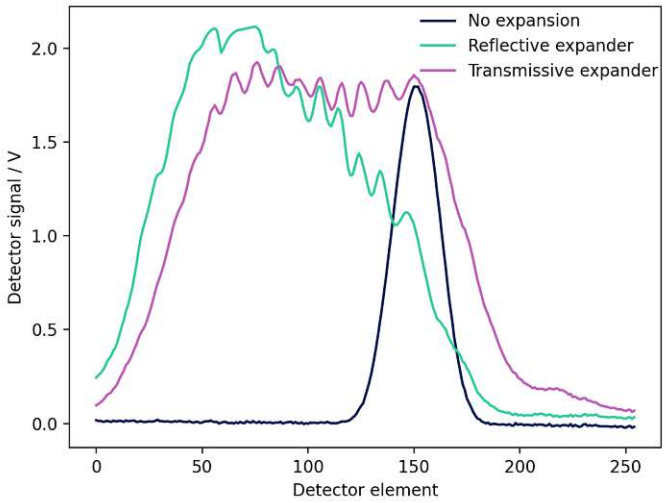

Figure 22: The signal, measured at each detector element both before (no expansion) and after the installation of beam-expanding components at a wavenumber of 1680 cm^{-1}. The reflective beam expander was constructed from fabricated mirrors, while two plano-convex lenses were utilized for the transmissive configuration. Both exhibited a pronounced interference pattern, which is likely attributable to reflections from the germanium window positioned in front of the detector.

As a subsequent step, a dilution series of caffeine in ethanol (between 2.5 and 25 mM) was prepared and measured with a flow cell of constant pathlength (102 µm). The measurements were conducted with the optimized parameters and setup as previously described in Section 3.2.1. However, to account for the beam expansion, the laser power was increased to 380 mA, which enabled the measurement across the full wavenumber spectrum of the laser without oversaturation of the detector. Figure 23A depicts the mean absorbance of three scans per concentration of detector element #100, which were subsequently smoothed using a Savitzky–Golay filter (polynomial fit of third order and a window size of 15 cm^{-1}). The regression model yielded a high coefficient of determination of 0.9993, indicating the successful applicability of the setup.

As documented in literature, caffeine exhibits two distinct absorption bands when analyzed in a D_2O solution, with the first band positioned between 1700 and 1692 cm^{-1} and the second between 1647 and 1641 cm^{-1}.[57] These bands can be attributed to the isolated and conjugated C=O stretching, respectively. However, when measuring the test solutions of caffeine in ethanol, it is notable that the band peaks exhibit a slight shift to higher wavenumbers, with the first band appearing at 1716 cm^{-1} and the second at 1662 cm^{-1}. This can be attributed to the effect of the solvent, given that hydrogen-bonded bands are highly sensitive to the solvent environment. Furthermore, additional wavenumber shifts are

observed due to the dimerization of caffeine in aqueous solutions, depending on the concentration. To demonstrate this phenomenon, a spectrum of caffeine in ethanol, chloroform, and water was recorded with a FT-IR spectrometer in transmission mode for comparison. The spectra are presented in Figure 23B, with the absorbance values normalized to the band at approximately 1650 cm^{-1}.

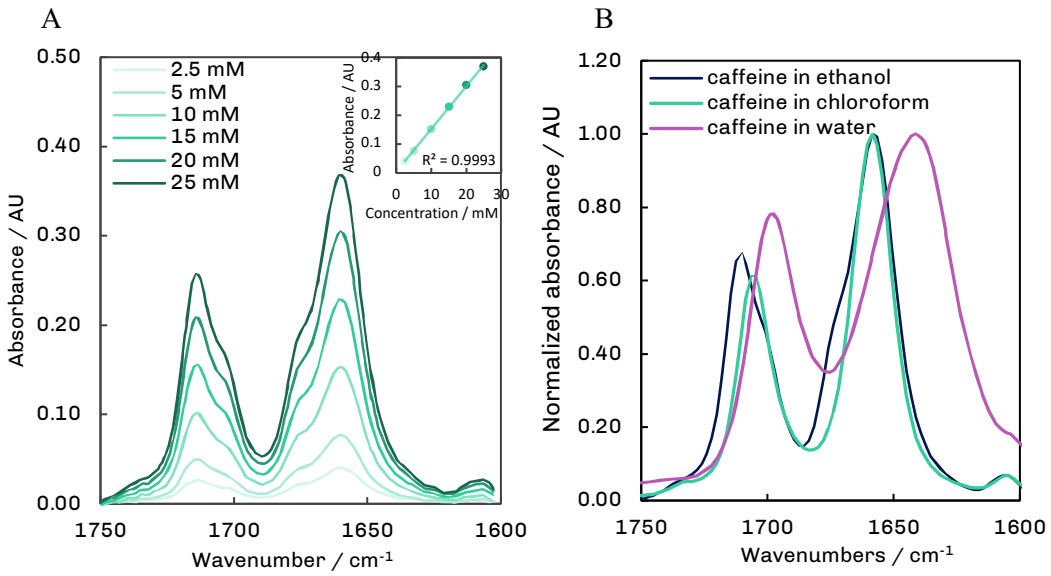

Figure 23: Absorbance spectra of a dilution series of caffeine in ethanol at a constant pathlength (A). Normalized FT-IR spectra of caffeine in different solvents (B).

3.2.3 Installation of the Multi-Pathlength Transmission Cell and Pathlength Calibration

In order to install the wedged-shaped transmission cell, a spacer with a thickness of 12 µm was utilized, and the cell was assessed for any potential leakage. Once more, caffeine in ethanol was employed as the test substance to ascertain whether the cell was functioning as anticipated. However, in order to proceed with the custom-made cell, it was essential to determine which detector element corresponded to which pathlength within the wedged-shaped cavity. The application of the interference fringe method was not possible due to the inherent limitations of focusing the beam to such a small spot within the wedged-shaped transmission cell. Moreover, the windows within the cavity do not represent two parallel surfaces due to the wedged shape of the cell. Accordingly, an external calibration method was selected, necessitating the assessment of the test solution with cells of varying pathlengths. Subsequently, spacers of four different thickness (between 12 and 104 µm) were placed in the constant pathlength transmission cell and the precise pathlength was determined through FT-IR with the interference fringe method. Subsequently, the absorbance spectra of caffeine in ethanol (5–15 mM) were recorded with the EC-QCL-

based setup at these pathlength, and a regression curve was created using the absorbance maximum at 1662 cm^{-1} (see Figure 24A). Then, the multi-pathlength cell was reinstalled, and the absorbance of the same standard solution was measured to determine the respective pathlengths for each detector element. This was done successfully, and each detector element could be allocated to a specific pathlength. Figure 24B also shows that due to the placement of the cell in front of the detector, the first 43 detector elements are not illuminated.

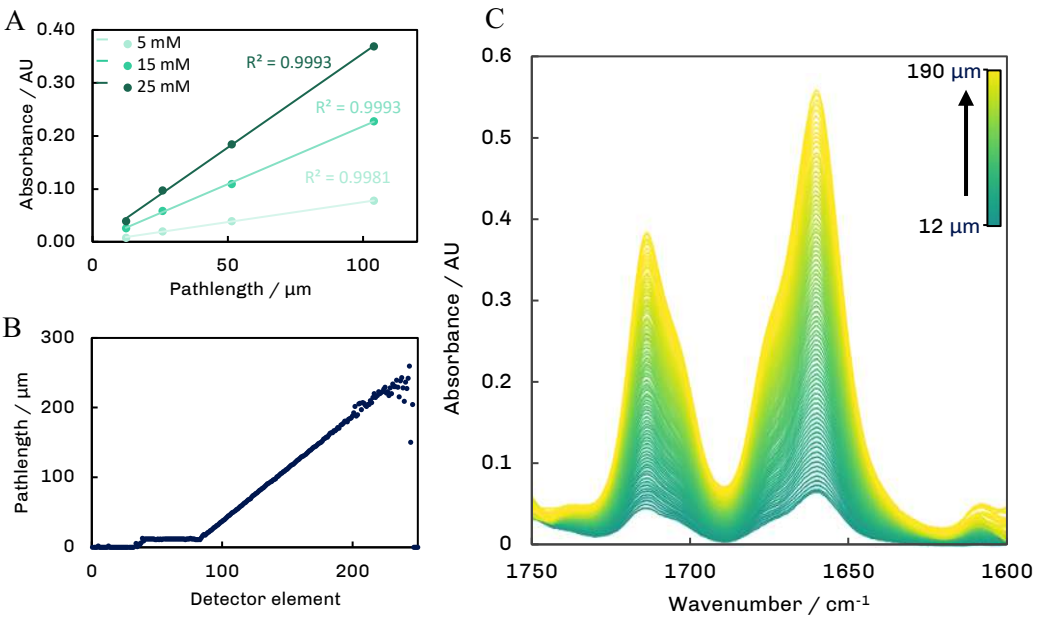

Figure 24: Caffeine in ethanol was measured at four different known pathlengths between 12 and 104 µm and a regression model was created with the absorbance maximum at 1662 cm^{-1}(A). With that, a calibration of the pathlength of the wedged-shaped transmission cell could be performed (B). Therefore, it was possible to know which detector element corresponds to which pathlength. The absorbance spectra recorded with each detector element shows the linear relationship between the absorbance and the pathlength. The spectrum shows the absorbance of caffeine in ethanol (20 mM)(C).

3.3 Development of a Post-processing Method for Unevenly Absorbing Matrices

Ultimately, following the successful testing of the setup with evenly absorbing matrices, the next stage of the process involved the analysis of aqueous solutions. Initially, a dilution series of caffeine in water (concentrations between 5 and 25 mM) was prepared and the solutions were injected into the flow cell via a syringe. It should be noted that great caution was required to prevent the injection of air bubbles, which could remain in the cell and result in the loss of data. Given that water is more prone to leakage due to its lower viscosity, it was necessary to ensure that the cell was completely tight. Furthermore, the

distinction between matrices with minimal absorption, such as ethanol, and highly absorbing solvents, like water, had to be made when selecting the experimental settings. To obtain a sufficient signal in the water bending region and at the lowest pathlengths, the highest laser power of 650 mA was employed. For caffeine in ethanol, satisfactory spectra could be generated for all recorded pathlengths. This was not the case for aqueous solutions as the detector elements were partially saturated or detected no radiation depending on the spectral region. Since all pathlengths were recorded for every scan, the challenge lay in developing a method to use solely the signals which are in the dynamic range of the detector.

3.3.1 Selection of the Optimal Pathlength for a Specific Spectral Region

The initial approach entailed the selection of the optimal pathlength for a specific wavenumber region, depending on the background absorbance. The wavenumber regions of highest interest were selected based on the peak positions of the absorbance bands of the analyte. In the case of caffeine, the two band maxima at 1698 cm^{-1} and 1642 cm^{-1} were selected, with the former exhibiting less interference from the aqueous solvent than the latter.

The 100% line was calculated from the background scans that were recorded prior to each measurement series. The RMS noise was determined for each spectrum of the detector elements, by calculating the standard deviation of the 100% line within a range of 20 cm^{-1} around the positions of the absorbance bands of the analyte. Subsequently, the signals from the sample measurements that were saturated or zero were excluded from the analysis, and the absorbance was determined. The maximum values of the bands were selected as the signal for the SNR calculations. A SNR threshold was established for both regions, after which the spectrum was designated as satisfactory. Subsequently, the most optimal pathlength was selected from the aforementioned spectra based on the SNR and the shape of the bands. The two spectra were then merged, as illustrated in Figure 25.

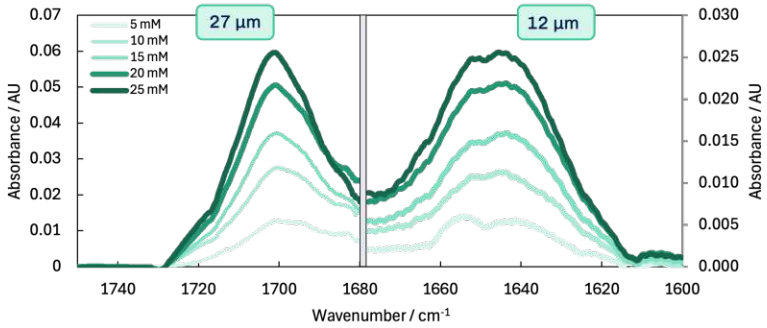

Figure 25: The first approach to analyze the absorbance spectra of caffeine in water. Specific pathlengths were selected based on the SNR to depict specific regions of the spectrum.

However, this method was found to be cumbersome due to the necessity of selecting the wavenumber regions for which the signal-to-noise ratio should be optimized based on the absorbance spectrum of the analyte. Moreover, only one of the 256 measured scans (one from each detector element) was selected for the final plotting of the spectrum.

3.3.2 The Pathlength-to-Noise Ratio as a Metric for Spectral Averaging

An alternative approach was adopted, whereby the noise was calculated in the time domain. This required recording multiple background scans and calculating the 100%-line from two consecutive measurements at a time. Subsequently, the RMS noise for each pathlength (detector element) and wavenumber is calculated based on the generated 100%-lines. The RMS noise is illustrated in Figure 26. The white regions indicate instances where the detector was either oversaturated or exhibited no signal due to the total absorption of the incident beam by the solvent. It is evident that shorter pathlengths are necessary in the region associated with the water bending mode at approximately 1645 cm^{-1}. The detector elements between #45 and #85 are all equivalent to a pathlength of 12 µm, which was defined by a spacer thickness. It is shown that the lowest noise levels are observed at short pathlengths. Additionally, the fringes resulting from the germanium window positioned in front of the detector elements, have an influence on the noise and the characteristic pattern can also be found in the noise map.

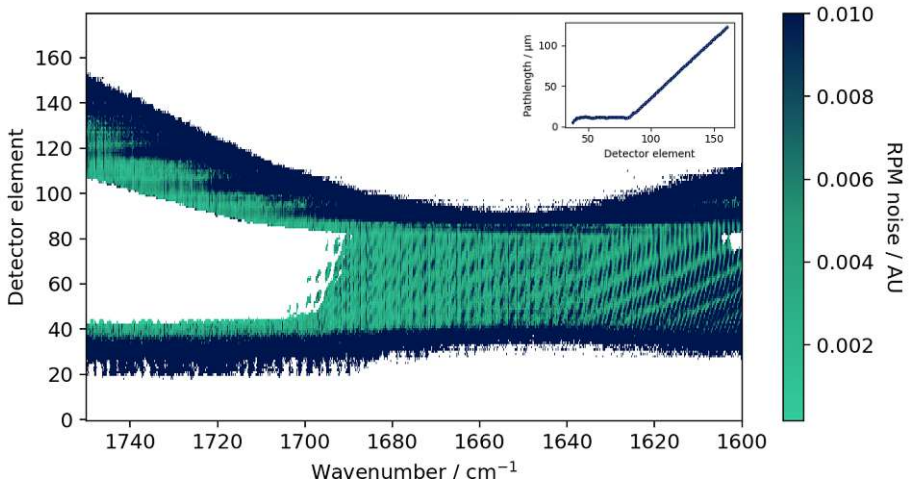

Figure 26: The RMS noise across the covered wavenumber region and the detector elements. The detector elements between #45 and #85 all correspond to a pathlength of 12 µm, whereas the pathlength increased to a pathlength of 110 µm at detector element #150.

Subsequently, a weighting scale was implemented for the purpose of automatically evaluating the optimal signal out of all measured detector elements for each wavenumber. Rather than utilizing the SNR, which is dependent on the analyte absorbance, which is not

constant across the entire wavelength range under consideration, a new term is introduced: The pathlength-to-noise ratio (PNR).

$$PNR = \frac{d}{s_{bl}} \qquad \text{Equation 20}$$

As previously discussed in Section 1.3.2, the SNR can also be used to characterize a spectrometer for which 100% transmission represents the signal value. This could also be done for the calculation of the SNR in this instance; however, it would not include the influence of the variable pathlength on the detectability of a substance. As the Beer-Lambert law describes, the absorbance signal has a linear dependence on the pathlength. Consequently, a higher PNR would also give a higher SNR, without the need of defining the signal itself. The advantage of coining this term is that it combines the effects of both pathlength and noise into a single metric, which could then be used as a weighing scale for the absorbance spectra. The representation of the PNR can be seen in Figure 27.

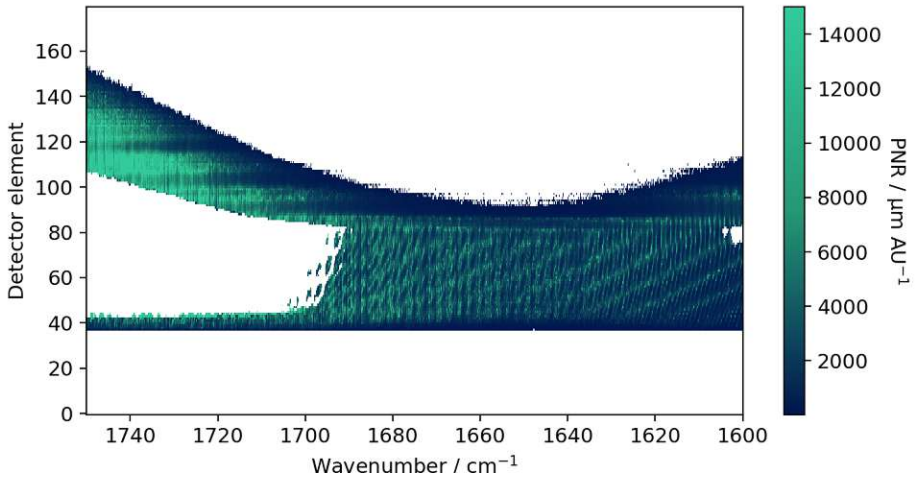

Figure 27: The pathlength-to-noise ratio across the covered wavenumber region and the detector elements. The detector elements between #45 and #85 all correspond to a pathlength of 12 µm, whereas the pathlength increased to a pathlength of 110 µm at detector element #150.

To use this metric for the evaluation of the absorbance data, the following post-processing steps have been taken (see Figure 28): First of all, the raw data were filtered by removing saturated detector signals or such which showed no signal for both background and sample measurements. The background scans were then averaged and the absorbance of each sample scan for each detector element was calculated. Subsequently, the absorbance spectra were averaged as well and the absorbance values were normalized by the pathlength at which they were recorded (determined according to Section 3.2.3). All 256 spectra from one measurement are then combined by the weighted arithmetic mean, with each

contributing to the resulting spectrum based on the PNR determined for each wavenumber and detector element. The unit of the resulting absorbance spectrum is therefore AU µm^{-1} and the value is dependent solely on the concentration.

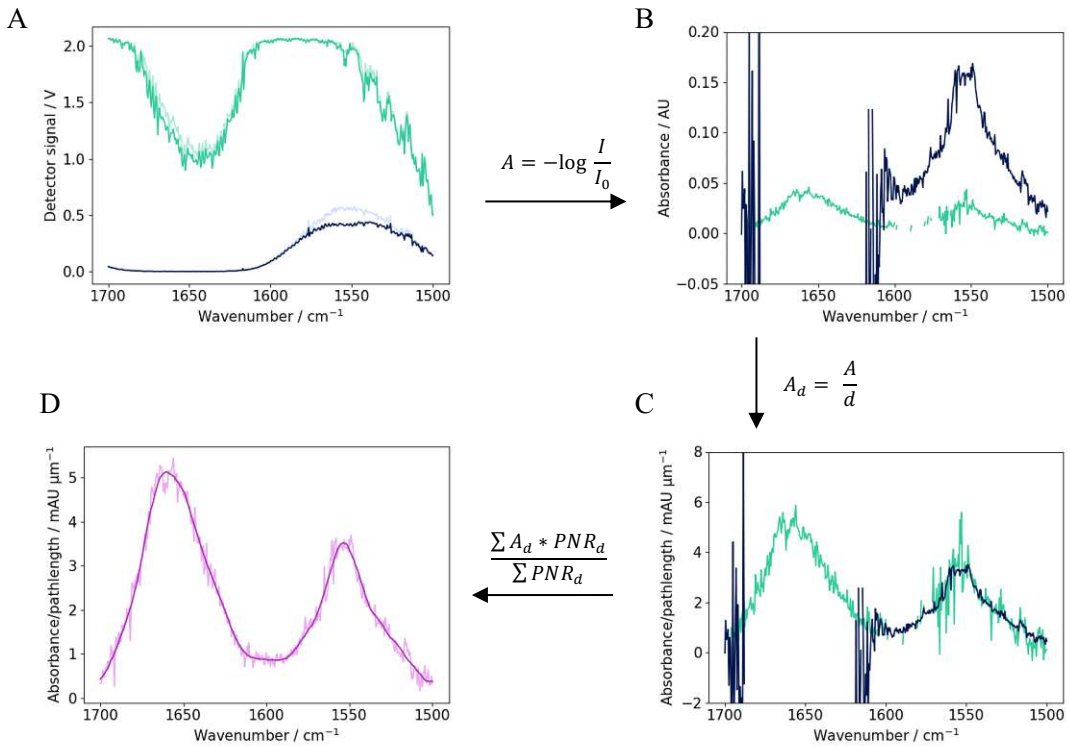

Figure 28: The post processing steps illustrated using the recorded signals of two different pathlengths (7.4 µm (green) and 48 µm (blue)) (A). The absorbance is calculated for every recorded pathlength separately according to the Beer-Lambert law (B). Then, the absorbance is normalized by the pathlength (C). All spectra are then averaged with the weighted mean based on the PNR value of each detector element at each wavenumber. The resulting spectrum is then smoothed with a Savitzky-Golay filter (D).

In the following graph, the absorbance spectra of caffeine in aqueous solutions are depicted. After the procedure described above the spectra were further smoothed with a Savitzky-Golay filter of third-degree order and a window size of 25 cm^{-1}. The limit of detection was calculated by normalizing the noise for each detector element with the pathlength as well and calculation of the averaged noise per pathlength with the PNR as weighing matrix. The noise at wavenumber of the band maxima were then divided by the sensitivity calculated with each regression curve. The limit of detection for caffeine in ethanol for wavelength 1646 cm^{-1} is therefore 11.4 mM, whereas for 1702 cm^{-1} it is 9.21 mM. This shows that the lowest two measured concentration are under the limit of detection for the spectral region in which water absorbs strongly.

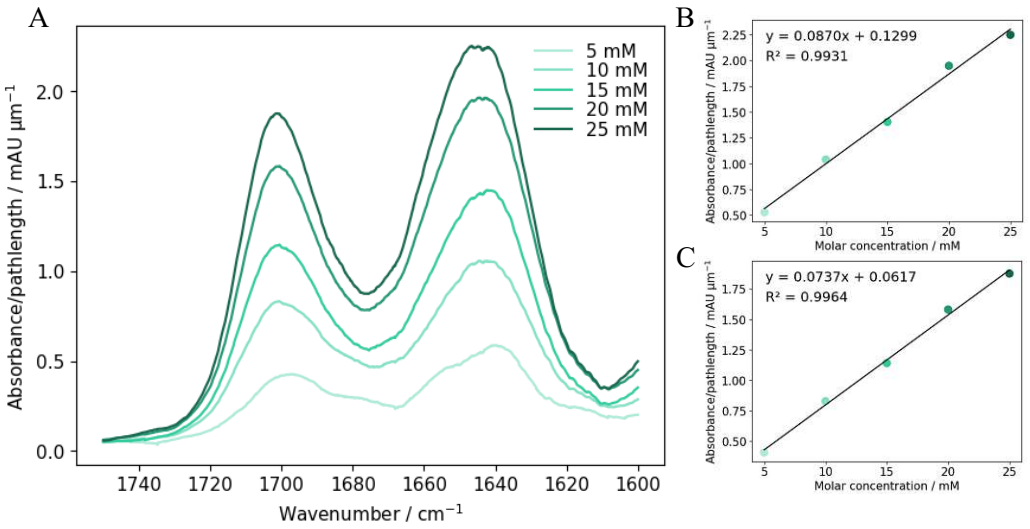

Figure 29: Spectra of caffeine in water calculated by weighted average of the absorbance at different pathlengths(A). A regression curve was created for the band maxima at 1646 cm^{-1}(B) and at 1702 cm^{-1} (C).

To demonstrate the efficacy of this post-processing technique, three 100% lines of water are presented in Figure 30 as examples. Figure 30A illustrates the absorbance at a pathlength of 48 µm. It is evident that in the region where the water bending vibration occurs, no signal was detected as a result of complete solvent absorption. In regions where only a minimal amount of radiation was detected, the noise level was exceedingly high. However, in areas with low solvent absorption, the noise values were substantially reduced due to the high pathlength. In comparison, the 100% line recorded with a pathlength of 7.4 µm (see Figure 30B) covers the region of the water bending vibration, while no absorption value could be calculated for the adjacent region due to the detector being oversaturated. To obtain a 100% line of the entire tuning range of the laser, the calculated absorbance for each detector element was divided by the pathlength and averaged for each wavenumber using a weighted mean based on the PNR. As illustrated in Figure Figure 30C, the noise in the region of the water bending vibration is lower than in the single pathlength measurement, while low noise levels are maintained compared to the measurement at a high pathlength.

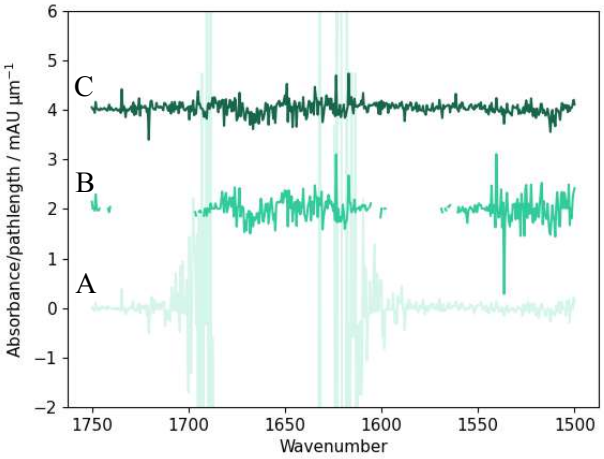

Figure 30: Comparison of 100% lines recorded at a single large pathlength of 48 µm (A), a single small pathlength of 7.4 µm (B) and the 100% line calculated by the weighting average of all recorded detector elements (C).

3.3.3 Measurement of Proteins in Aqueous Solution

Following the development of the measurement and evaluation script, as outlined in Section 3.3.2, the laser head was replaced with one operating in the 1798–1488 cm^{-1} range, allowing for the measurement of protein. Moreover, the spacer in the multi-pathlength transmission cell was replaced with a thinner one of 7 µm to more accurately account for the measurement of water as a highly absorbing matrix, as previous measurements have demonstrated that 12 µm was already the maximum pathlength for certain spectral regions.

With the introduction of the new spacer, it was necessary to recalibrate the pathlengths of the cell. This involved remeasuring caffeine in ethanol and correlating the absorbance maxima at each detector element to the maxima measured with the fixed-pathlength cell. The calibration demonstrated that the cell had a pathlength of 7.4 µm at the thinnest point. The minimal thickness of the cell required the application of a relatively high pressure to facilitate the flow of liquid through the cell and tubing. This increased the probability of leakage.

Subsequently, a series of background measurements were performed in order to calculate the RMS noise. The PNR was subsequently determined in accordance with the previously described method (see Section 3.3.2), and the resulting data are presented in Figure 31.

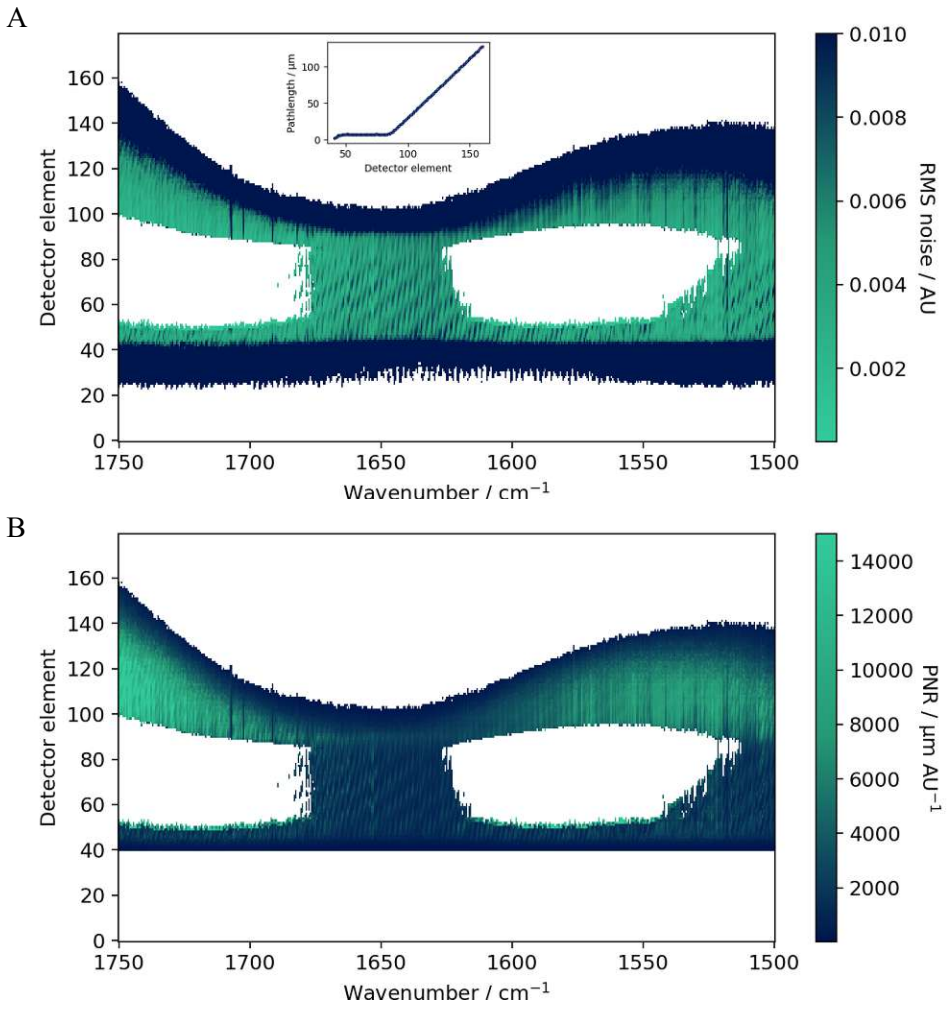

Figure 31: The RMS noise (A) and pathlength-to-noise ratio (B) across the covered wavenumber region and the detector elements. The detector elements between #45 and #85 all correspond to a pathlength of 7.4 µm, whereas it then increases up to a pathlength of 106 µm at detector element #150.

Finally, BSA was measured with the above settings, resulting in the spectra shown in Figure 32. It shows the absorbance versus pathlength for BSA concentrations between 1 and 50 mg mL^{-1} for the wavenumber range between 1500 and 1700 cm^{-1}. It also shows a regression model built from the absorbance maximum at 1660 cm^{-1} with a high R^2 value of 0.9996 for the amide I band, indicating a good fit. Most importantly, the amide I and amide II bands are clearly identifiable in the presented measurement, allowing accurate qualification and quantification of the protein under investigation. With respect to the 1 mg mL^{-1} BSA concentration, it should be noted that although the characteristic amide I and amide II bands are easily visible, a concentration of at least 5 mg mL^{-1} appears to be required for reliable identification of BSA. This could also be shown by calculation of the limit of detection

which resulted in a limit of detection of 7.81 mg mL^{-1} for the amide I band and 3.98 mM for the amide II band. The demonstration of this final measurement of protein in water marks the conclusion of the developments presented in this thesis.

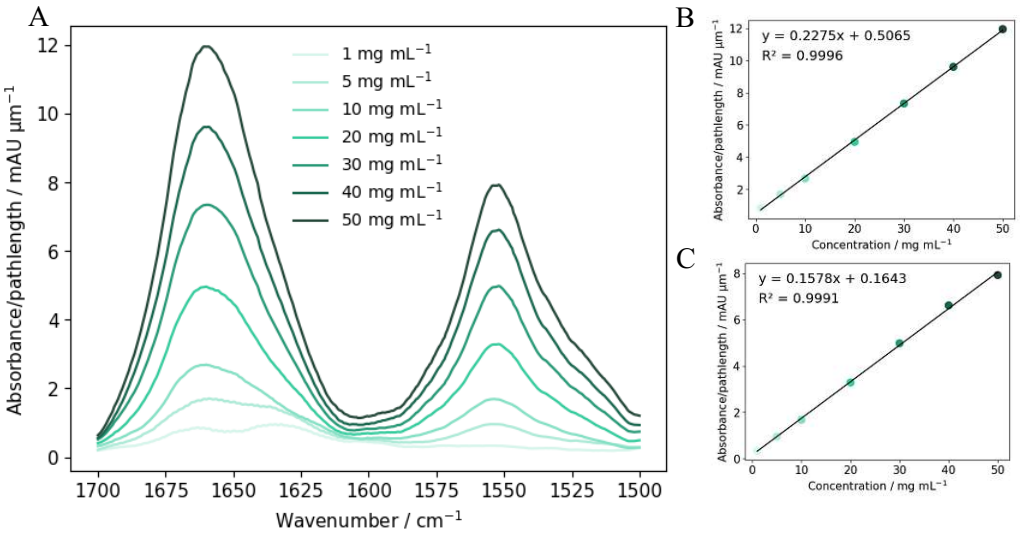

Figure 32: Spectra of BSA in water calculated by weighted average of the absorbance at different pathlengths (A). A regression curve was created for the band maxima at of the amide I (B) and the amide II band (C).

4 Conclusion and Outlook

This work introduced and successfully tested a novel EC-QCL based multi-pathlength spectroscopic setup equipped with a wedge-shaped transmission flow cell and a pyroelectric array detector. The ability to simultaneously measure across multiple pathlengths offers a flexible solution for the analysis of samples with varying absorbance. The setup was equipped with an external cavity quantum cascade laser as the radiation source as it allowed for the precise tunability over the mid-IR region of interest which further increases the ability of the setup to accommodate highly absorbing matrices without the need for labor intensive dilutions. The concept of a wedge-shaped transmission cell was proven by showing its ability to creating an output which depends linearly on the place of the detector element. The limiting dynamic range of the pyroelectric detector used in the setup could be mitigated as the simultaneous measurement of multiple pathlengths allowed for the effective dynamic range of the setup, to be increased by allowing the data to be selected for each wavenumber with a distinct pathlength and corresponding suitable intensity at the detector. This selection was made based on a newly introduced metric, the PNR (pathlength-to-noise ratio). This parameter quantifies the enhanced sensitivity that can be achieved at higher pathlengths, while including the impact of noise and therefore the limit of detection. The PNR was utilized as a weighting metric to calculate the weighted average of the absorbance recorded by each detector element at each wavenumber.

The setup was constructed from its basic components, with the initial stage consisting of the design of the custom-built flow cell, the characterization of the laser beam parameters, and the electronic connection of the detector with the chopper and the TEC sensor. Moreover, a Python script was developed to enable the measurements, which were controlled via laptop. Once each component had been mounted and evaluated, the next step was to perform the first measurement and assess the optimal measurement parameters. A preliminary test substance, caffeine in ethanol, was used for this purpose. Subsequently, the optical pathlength of each detector element was aligned with the measured value. A Python script was developed to automatically select the optimal pathlengths based on the pathlength-to-noise ratio. The performance of the setup with an unevenly absorbing matrix was demonstrated by measuring BSA in aqueous solution. The objective was to illustrate how this approach can enhance the sensitivity, flexibility, and accuracy of liquid-phase IR spectroscopy while mitigating the limitations posed by highly absorbing solvents.

Besides showing the potential, some limitations of the setup were also observed, which could be starting points for future work trying to improve on the demonstrated concept. Starting with the cell design, the pathlength range of 400 µm proved to be too broad for water-based solutions as the maximum usable pathlength was significantly below 400 µm. Furthermore, due to the design regarding the location of the tubing holes determined by the

small size of the cell, there was very little space between the tubing ports and the alignment pins which made assembly of the cell quite challenging. Given that the cell was already rather prone to leakage due to the relatively high pressures and the difficulty of obtaining tighter manufacturing tolerances, the difficult assembly often lead to additional leakage problems. For future iterations a redesign, which has better sealing capability and allows for easier assembly would be desirable.

Besides the cell design additional improvements to the setup can be made, for example adding an apodization filter to further improve the performance of the beam expander by enhancing the beam uniformity. Furthermore, the germanium window mounted in front of the detector element led to interference fringes, which were observable in the noise pattern of the measurement results. These interference patterns can lead to deviations from the linearity of the Beer-Lambert law. To avoid these interferences, it would therefore be beneficial to remove the germanium window in a future iteration.

In conclusion, this work demonstrates the potential of the presented multi-pathlength mid-IR spectroscopy setup by showing its potential benefit over a fixed pathlength setup. While improvements to the physical setup design as well as data processing are necessary, this work can serve as a foundation for future projects to further refine on these aspects and to broaden the spectrum of analyzed substances. This can lead to enhancing the understanding of this spectroscopy concept and to determine if this technology could be of further used in both research and industry.

5 List of Figures

6 References

The text was reviewed and corrected for grammatical accuracy using DeepL's writing tools.

1 Griffiths, P. R. & De Haseth, J. A. *Chemical analysis; v. 171* (Wiley-Interscience, Hoboken, N.J., 2007).

2 Ozaki, Y. Infrared Spectroscopy: Mid-infrared, Near-infrared, and Far-infrared/Terahertz Spectroscopy. *Anal Sci* **37**, 1212, doi:10.2116/analsci.20R008 (2021).

3 Morse, P. M. Diatomic Molecules According to the Wave Mechanics. II. Vibrational Levels. *Physical Review* **34**, 57-64, doi:10.1103/PhysRev.34.57 (1929).

4 Thompson, J. M. *Infrared Spectroscopy*. 1 edn, (Jenny Stanford Publishing, 2018).

5 Hsu, C.-P. S. Infrared spectroscopy. *Handbook of instrumental techniques for analytical chemistry* **249** (1997).

6 Stephens, E. R. Long-path infrared spectroscopy for air pollution research. *Infrared Physics* **1**, 187-196, doi:https://doi.org/10.1016/0020-0891(61)90022-7 (1961).

7 Schwaighofer, A., Brandstetter, M. & Lendl, B. Quantum cascade lasers (QCLs) in biomedical spectroscopy. *Chemical Society Reviews* **46**, doi:10.1039/C7CS00403F (2017).

8 Mayerhöfer, T. G. & Popp, J. Beer's Law – Why Absorbance Depends (Almost) Linearly on Concentration. *ChemPhysChem* **20**, 511-515, doi:https://doi.org/10.1002/cphc.201801073 (2019).

9 Mayerhöfer, T. G., Pahlow, S. & Popp, J. The Bouguer-Beer-Lambert Law: Shining Light on the Obscure. *ChemPhysChem* **21**, 2029-2046, doi:https://doi.org/10.1002/cphc.202000464 (2020).

10 Mayerhöfer, T. G., Pahlow, S. & Popp, J. Understanding the Limits of the Bouguer-Beer-Lambert Law. *Spectroscopy*, 29-30,58, doi:10.56530/spectroscopy.iq2368r9 (2023).

11 Aryal, S. Beer-Lambert Law- Definition, Derivation, and Limitations. (2022).

12 Dabrowska, A., Lindner, S., Schwaighofer, A. & Lendl, B. Mid-IR dispersion spectroscopy – A new avenue for liquid phase analysis. *Spectrochimica Acta Part A: Molecular and Biomolecular Spectroscopy* **286**, 122014, doi:https://doi.org/10.1016/j.saa.2022.122014 (2023).

13 Ball, D. W. *Field Guide to Spectroscopy*. (SPIE Press, 2006).

14 Bonani, F. & Ghione, G. in *Noise in Semiconductor Devices: Modeling and Simulation* (eds Fabrizio Bonani & Giovanni Ghione) 1-38 (Springer Berlin Heidelberg, 2001).

15 Agilent Technologies. Highest available Signal-To-Noise performance, delivering superior sensitivity and analytical performance. (2011).

16 Long, G. & Winefordner, J. D. Limit of detection. A closer look at the IUPAC definition. *Analytical Chemistry* **55**, doi:10.1021/ac00258a001 (2008).

17 Nomenclature, symbols, units and their usage in spectrochemical analysis—II. data interpretation. *Spectrochimica Acta Part B: Atomic Spectroscopy* **33**, 241-245, doi:https://doi.org/10.1016/0584-8547(78)80044-5 (1976).

18 Mocak, J., Bond, A. M., Mitchell, S. & Scollary, G. A statistical overview of standard (IUPAC and ACS) and new procedures for determining the limits of detection and quantification: Application to voltammetric and stripping techniques (Technical Report). **69**, 297-328, doi:doi:10.1351/pac199769020297 (1997).

19 Thomsen, V., Schatzlein, D. & Mercuro, D. in *Spectroscopy* Vol. 18 112+ (2003).

20 Little, T. A. Method Validation Essentials, Limit of Blank, Limit of Detection, and Limit of Quantitation. *BioPharm International* **28**, 48-51 (2015).

21 Boumans, P. W. J. M. & De Boer, F. J. Studies of flame and plasma torch emission for simultaneous multi-element analysis—I: Preliminary investigations. *Spectrochimica Acta Part B: Atomic Spectroscopy* **27**, 391-414, doi:https://doi.org/10.1016/0584-8547(72)80038-7 (1972).

22 Verma, P. K. *et al.* The Bend+Libration Combination Band Is an Intrinsic, Collective, and Strongly Solute-Dependent Reporter on the Hydrogen Bonding Network of Liquid Water. *The Journal of Physical Chemistry B* **122**, 2587-2599, doi:10.1021/acs.jpcb.7b09641 (2018).

23 Schwaighofer, A. *et al.* Beyond Fourier Transform Infrared Spectroscopy: External Cavity Quantum Cascade Laser-Based Mid-infrared Transmission Spectroscopy of Proteins in the Amide I and Amide II Region. *Analytical Chemistry* **90**, 7072-7079, doi:10.1021/acs.analchem.8b01632 (2018).

24 bartleby. *IR Spectrum Of Anisole* https://www.bartleby.com/subject/science/chemistry/concepts/ir-spectrum-of-anisole

25 Schwaighofer, A. & Lendl, B. in *Inclusion Bodies: Methods and Protocols* (eds Julian Kopp & Oliver Spadiut) 209-223 (Springer US, 2023).

26 Dabrowska, A. *Development and Application of Mid-IR Dispersion Spectroscopy for Chemical Analyisis in the Liquid-Phase* Doctor of Technical Sciences thesis, Technische Universität Wien, (2022).

27 Michelson, A. A. & Morley, E. W. On the relative motion of the Earth and the luminiferous ether. *American Journal of Science* **s3-34**, 333-345, doi:10.2475/ajs.s3-34.203.333 (1887).

28 Schrader, B. in *Infrared and Raman Spectroscopy* (ed Bernhard Schrader) 1-5 (1995).

29 What is a Globar? *AZoOptics* (2013).

30 Neves, M. M. *et al.* Perspectives of FTIR as Promising Tool for Pathogen Diagnosis, Sanitary and Welfare Monitoring in Animal Experimentation Models: A Review Based on Pertinent Literature. *Microorganisms* **12** (2024).

31 Brown, S. Analysis of the State of the Art: Infrared Spectroscopy. **30** (2015).

32 Faist, J. *et al.* Quantum Cascade Laser. *Science* **264**, 553-556, doi:10.1126/science.264.5158.553 (1994).

33 *QUANTUM CASCADE LASER BASICS* https://www.teamwavelength.com/quantum-cascade-laser-basics/

34 Quantum Optoelectronics Group. *The Quantum Cascade Laser*, https://qoe.ethz.ch/Tutorials/quantum_cascade_laser.html

35 Yoon, Y. *et al.* Time resolved characterization of Fabry-Perot quantum cascade lasers for use in a broadband “white light” source. *Opt. Express* **27**, 32609-32620, doi:10.1364/OE.27.032609 (2019).

36 Paschotta, R. *Bragg Gratings*, https://doi.org/10.61835/8mq

37 Moser, H. *et al.* Application of a ring cavity surface emitting quantum cascade laser (RCSE-QCL) on the measurement of H2S in a CH4 matrix for process analytics. *Opt. Express* **24**, 6572-6585, doi:10.1364/OE.24.006572 (2016).

38 Hemingway, M. *External Cavity Quantum Cascade Lasers* (2018).

39 Gentec Electro-Optics. *The beginner's guide to laser beam quality and M2 measurement*, https://www.gentec-eo.com/blog/laser-beam-quality-measurement-m2 (2024).

40 Paschotta, R. *Beam Quality*, https://doi.org/10.61835/8mq

41 Prahl, S. *M² Experimental Design — laserbeamsize 2.0.5 documentation*, https://laserbeamsize.readthedocs.io/en/stable/13-M2-Experiment.html (2023).

42 Hossain, A. & Rashid, M. H. Pyroelectric detectors and their applications. *IEEE Transactions on Industry Applications* **27**, 824-829, doi:10.1109/28.90335 (1991).

43 Rogalski, A. *Infrared Detectors*. (CRC Press,, 2010).

44 Haller, E., Beeman, J., Hansen, W., Hubbard, G. & Jr, R. Pyroelectric detectors. (1990).

45 Hasegawa, T., Taniguchi, K. & Sato, Y. Selection of modulation frequency of FT-IR equipped with an MCT detector for thin-film analysis. *Vibrational Spectroscopy* **51**, 76-79, doi:https://doi.org/10.1016/j.vibspec.2008.10.018 (2009).

46 Odon, A. & Szlachta, A. Voltage Response of a Pyroelectric Detector to a Single Rectangular Optical Radiation Pulse. *Sensors* **22** (2022).

47 Stevenson, H. C., Wilson, P. V. & Pearce, K. A. WO2023007341 - AN IMPROVED SAMPLE HOLDER. USA patent (2021).

48 Repligen. *CTech™ SoloVPE® System*, https://www.repligen.com/solovpe

49 Robertson, C. W. & Williams, D. Lambert Absorption Coefficients of Water in the Infrared*. *J. Opt. Soc. Am.* **61**, 1316-1320, doi:10.1364/JOSA.61.001316 (1971).

50 Tyler, I. L., Taylor, G. & Querry, M. R. Thin-wedge-shaped cell for highly absorbent liquids. *Appl. Opt.* **17**, 960-963, doi:10.1364/AO.17.000960 (1978).

51 Wieliczka, D. M., Weng, S. & Querry, M. R. Wedge shaped cell for highly absorbent liquids: infrared optical constants of water. *Appl. Opt.* **28**, 1714-1719, doi:10.1364/AO.28.001714 (1989).

52 *Quantum Cascade Lasers (QCL) Frequently Asked Questions | What Is A QCL?*, https://www.daylightsolutions.com/technology/faq/

53 Prahl, S. *laserbeamsize*, https://laserbeamsize.readthedocs.io/en/latest/index.html (2023).

54 Dias Infrared. *Pyroelectric Linear Arrays PYROSENS*, http://www.dias-infrared.de/pdf/pyrosens_arrays_eng_mail.pdf (2024).

55 Edmund optics. *Laser Beam Expanders*, https://www.edmundoptics.com/knowledge-center/application-notes/lasers/beam-expanders/

56 Filizzola, C., Pergola, N. & Tramutoli, V. *The Rayleigh roughness criterion*, https://ltb.itc.utwente.nl/518/concept/92553

57 Falk, M., Gil, M. & Iza, N. Self-association of caffeine in aqueous solution: An FT-IR study. *Canadian Journal of Chemistry* **68**, 1293-1299, doi:10.1139/v90-199 (2011).

7 Appendix

7.1 Technical Drawing of the Front Cell

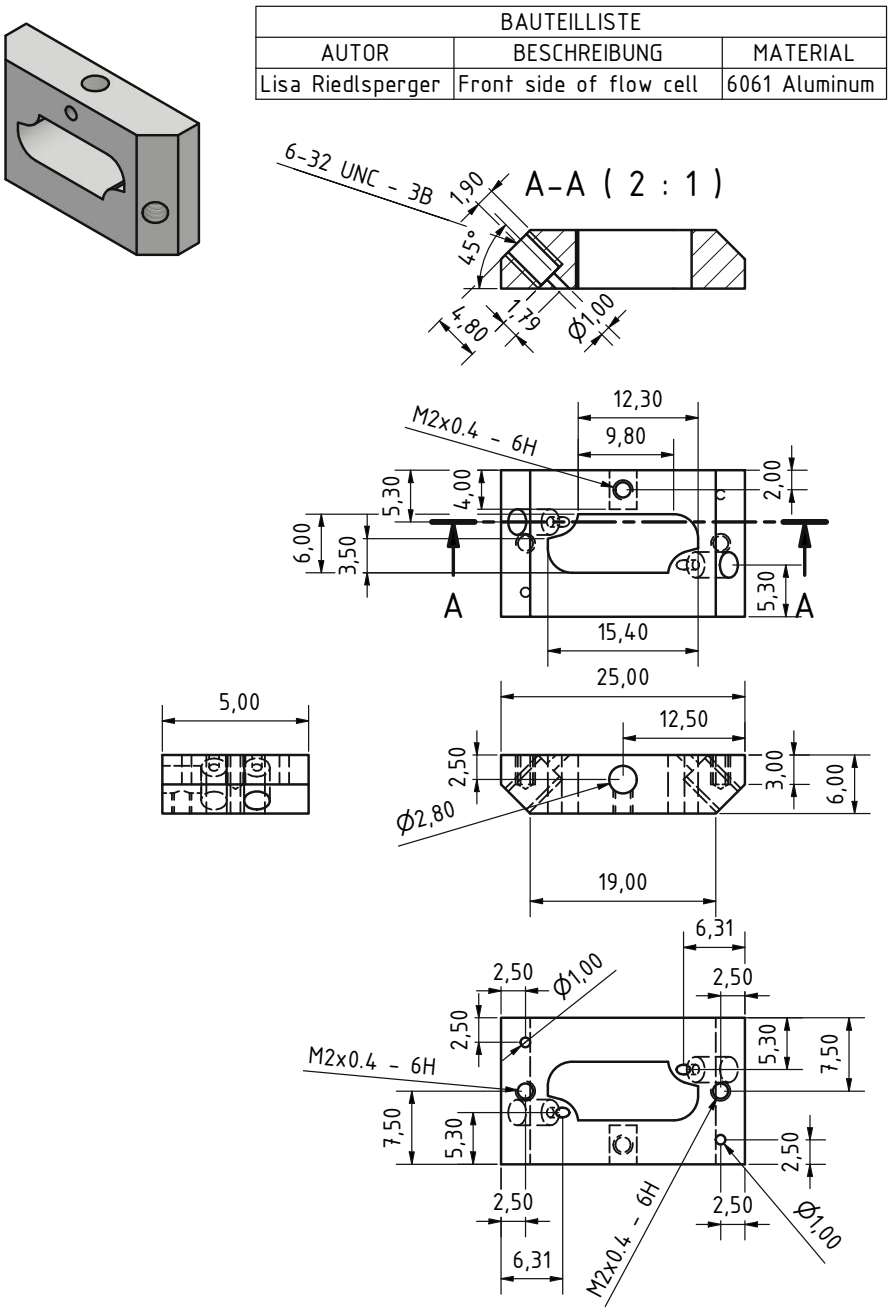

7.2 Technical Drawing of the Back Cell

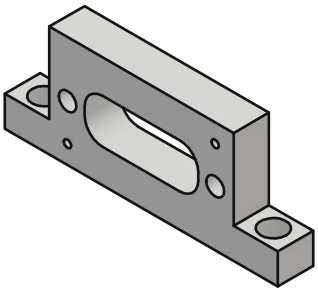

BAUTEILLISTE		
AUTOR	BESCHREIBUNG	MATERIAL
Lisa Riedlsperger	Back side of flow cell	6061 Aluminum

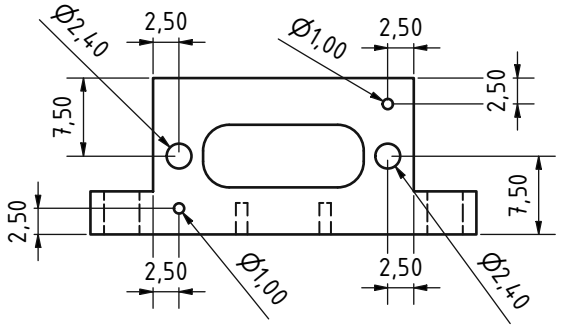

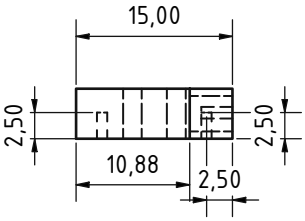

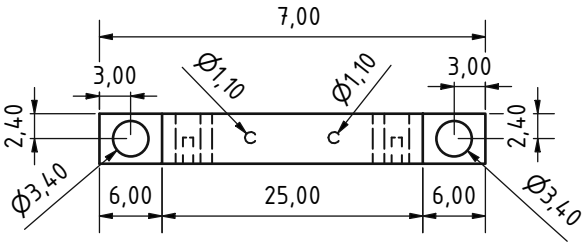

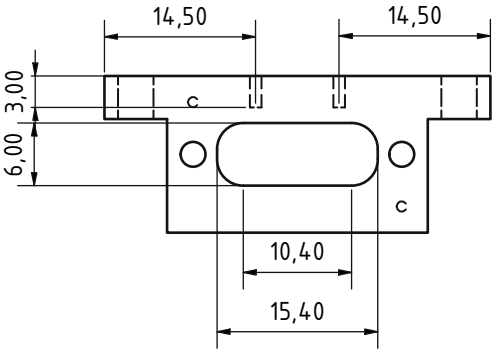

7.3 Technical Drawing of the Wedged-shaped Window

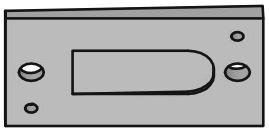

BAUTEILLISTE		
AUTOR	BESCHREIBUNG	MATERIAL
Lisa Riedlsperger	Wedged shaped cavity window	CaF2

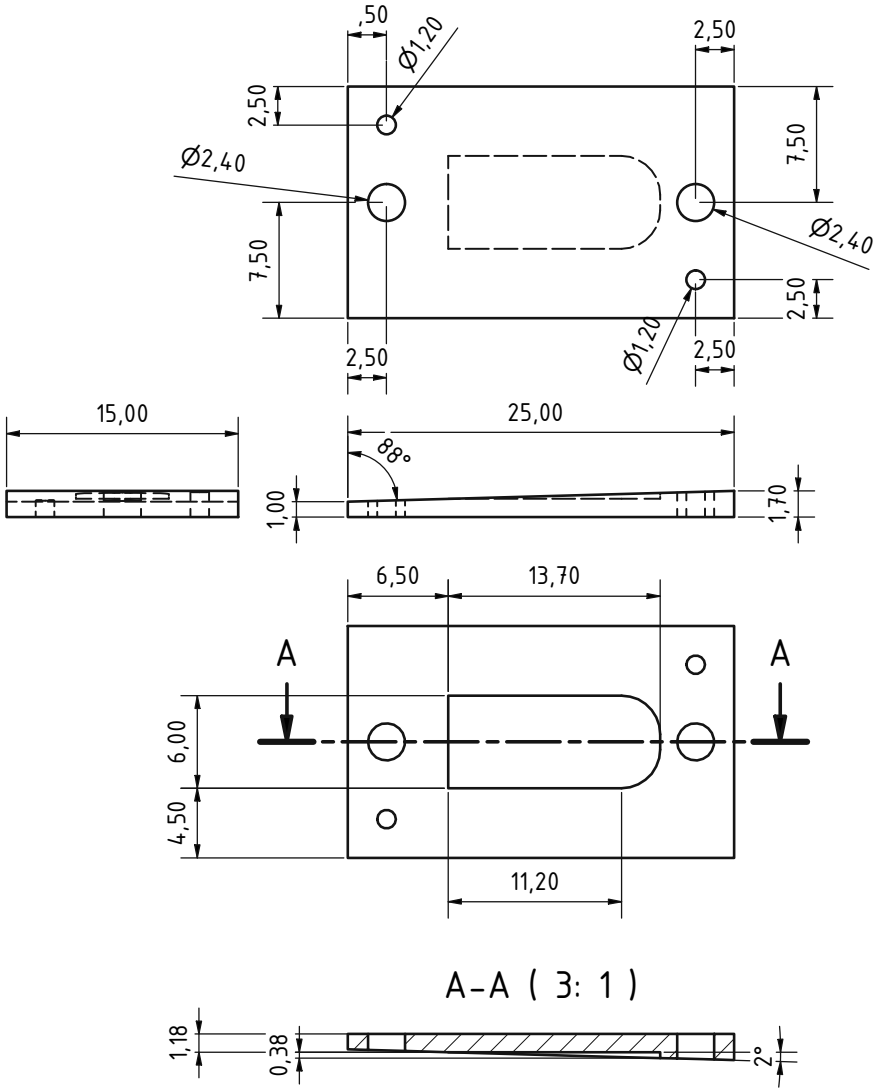

7.4 Technical Drawing of the Flat Window

BAUTEILLISTE		
AUTOR	BESCHREIBUNG	MATERIAL
Lisa Riedlsperger	Flat window	CaF2

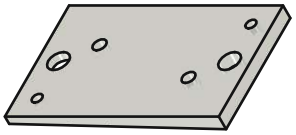

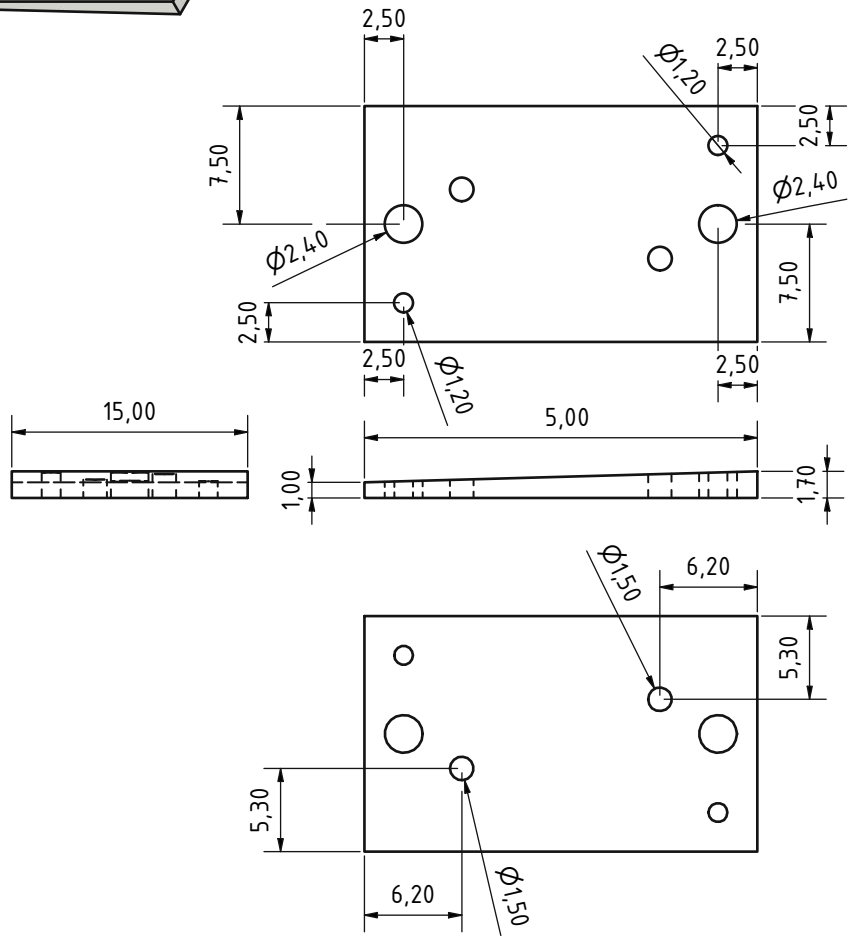

7.5 Python Script of the Measurement

```
## IMPORTS:

import time
import numpy as np
from sidekick import get_sidekick
kickl = get_sidekick()
import LISA_Control as ls
import ctypes
import datetime


## PARAMETERS:

#Laser
PULSE_WIDTH = 500 #ns
REPETITION_RATE = 100000 #Hz

step_size = 0.5 #cm-1
start_wn = 1500 #cm-1
stop_wn = 1700 #cm-1
current =700 #in mA

#Detector
Freq = 64 #Hz
VDR = 6725 #ns
VVR = 30 #ns
delay = 14600 #ns

Int = 1/ Freq *1000 - VDR/1000 #ms
current_date = datetime.date.today()

#Data Aquisition
file_name = f"{current_date}_{Freq}Hz_{Int}int_{VVR}VVR_{delay/1000}delay_{current}mA_{start_wn}-{stop_wn}cm-1"
output_file_name = file_name + ".txt"
offset_file_name = file_name +  "_offset.txt"
processed_file_name = file_name + "_proc.txt"

results = []
offset = []


## MEASUREMENT:

#Laser
kickl.setArmDisarm(True)
kickl.setLaserQclParams(REPETITION_RATE, PULSE_WIDTH, current)
kickl.setTuneToWW(start_wn)
kickl.emission_off()
time.sleep(3)

#Detector
def start_detector(VVR, VDR):

    print(ls.lisa_login())
    ls.setArraySize()
    ls.setSampleFreq(Freq)
    ls.setSyncexternal()
    ls.setSyncDelay(delay)
    ls.setSyncHighActive()
    print(ls.getSyncFreq())
    ls.setVVR(VVR)
    ls.setVDR(VDR)
    print(ls.getSensorTemp())
    ls.setStart()

start_detector(VVR, VDR)
```

```
# warmup scans
for i in range(3):
    values, error = ls.getPixelVoltages()
    current_temp = ls.getSensorTemp()
    print('Warm up:', error, current_temp)
    time.sleep(1)

#offset scans
for i in range(3):
    values, error = ls.getPixelVoltages()
    current_temp = ls.getSensorTemp()
    print('Background:', error, current_temp)
    offset.append([i , current_temp, values])
    time.sleep(1)

#turn Laser on
kickl.emission_on()
time.sleep(2)

#Measurement
while start_wn <= stop_wn:
    values, error = ls.getPixelVoltages()
    current_temp = ls.getSensorTemp()
    print(values[80])
    if error != 0 or current_temp < 2800 or values[1] < 1:
        print("The detector has been disconnected")
        print(ls.setStop())
        print(ls.lisa_logout())
        for i in range(3):
            start_detector(VVR, VDR)
            time.sleep(10)
            print("Trying to reconnect. Attempt " +i)
    else:
        results.append([start_wn , current_temp, values])
        print(start_wn)
        start_wn += step_size
        kickl.setTuneToWW(start_wn)
        time.sleep(0.4)

# Turn off laser
kickl.emission_off()
time.sleep(2)

#offset scans
for i in range(3,6,1):
    time.sleep(1)
    values, error = ls.getPixelVoltages()
    current_temp = ls.getSensorTemp()
    print('Background:', error, current_temp)
    offset.append([i , current_temp, values])


# Save raw data in txt file
with open(output_file_name, "w") as output_file:
    for wavenumber, current_temp, signals in results:
        pixel_number = 0
        for signal_value in signals:
            output_line = f"{wavenumber};{pixel_number};{current_temp}; {signal_value}\n"
            output_file.write(output_line)
            pixel_number += 1

print(f"Data has been saved to {output_file_name}")

# Save offset data in txt file
with open(offset_file_name, "w") as output_file:
    for i, current_temp, signals in offset:
        pixel_number = 0
        for signal_value in signals:
            output_line = f"{i};{pixel_number};{current_temp}; {signal_value}\n"
            output_file.write(output_line)
            pixel_number += 1
```

```
## Processing
# Calculate Offset

def calculate_averages(results):
    transposed_values = list(zip(*[measurement[2] for measurement in results]))
    averages = [sum(group) / len(group) for group in transposed_values]
    return averages

average_offset = calculate_averages(offset)

for i in offset:
    print(np.mean(i[2]))

corrected = results
for i in range(len(corrected)):
    for j in range(len(corrected[i][2])):
        corrected[i][2][j] = corrected[i][2][j] - average_offset[j]

# Save processed data in txt file
with open(processed_file_name, "w") as output_file:
    for i, current_temp, signals in corrected:
        pixel_number = 0
        for signal_value in signals:
            # Write each line in the format: wavenumber; pixel number; signal value
            output_line = f"{i};{pixel_number};{current_temp}; {signal_value}\n"
            output_file.write(output_line)
            pixel_number += 1
```